International Journal of Plasticity 30–31 (2012) 62–80

Contents lists available at SciVerse ScienceDirect

International Journal of Plasticity

journal homepage: www.elsevier.com/locate/ijplas

Probabilistic modeling of microstructure evolution using finite element representation of statistical correlation functions

V. Sundararaghavan *, A. Kumar

Aerospace Engineering, 3025 FXB Building, 1320 Beal Ave, University of Michigan, Ann Arbor, MI 48109, USA

ARTICLE INFO

Article history:
Received 19 June 2011
Received in final revised form 23 August 2011
Available online 10 September 2011

Keywords:
Microstructural descriptors
C. Numerical algorithms
B. Crystal plasticity
A. Microstructures
C. Probability and Statistics

ABSTRACT

A probabilistic finite element scheme is presented for simulating evolution of polycrystalline microstructures during deformation. The microstructure is described using conditional orientation correlation function (COCF), defined as the probability density of occurrence of a crystal orientation $\boldsymbol{g}'$ at a distance $\boldsymbol{r}$ from a given orientation $\boldsymbol{g}$. The COCF is represented using three interconnected layers of finite element meshes in the $\boldsymbol{g}'$, $\boldsymbol{r}$ and $\boldsymbol{g}$ spaces. As the microstructure evolves, the reoriented neighborhood and strain fields close to an orientation ($\boldsymbol{g}$) are captured by updating probability fields in these finite element meshes. For this purpose, a novel total Lagrangian approach has been developed that allows evolution of probability densities while satisfying normalization constraints, probability interdependencies and symmetries. The improvement in prediction of texture and strains achieved by the COCF approach over ODF-based methods is quantified through deformation analysis of a planar polycrystalline microstructure.

1. Introduction

Integrated computational materials engineering (ICME) (Allison et al., 2006; McDowell, 2010) is an emerging paradigm for materials design that emphasizes integration of material models at multiple length scales with engineering analysis of products and processes. For example, during simulation of metal forming processes, microstructure evolution can be explicitly tracked to facilitate design of optimized processing paths (Sundararaghavan and Zabaras, 2008). Such simulations have been successfully enabled through a combination of polycrystal plasticity theory and finite element analysis of polycrystalline aggregates (Harren and Asaro, 1989; Bronkhorst et al., 1992; Becker and Panchanadeeswaran, 1995; Beaudoin et al., 1996; Sarma et al., 2002). Here, microstructure evolution in the form of reorientation of crystals (texturing) is modeled by deforming an aggregate of grains characterized using microdiffraction techniques (Qidwai et al., 2009). There are two primary issues when dealing with finite element modeling of microstructures. Firstly, multiscale simulations that use finite element representation of the underlying microstructure are computationally prohibitive. Secondly, finite element simulations are deterministic while polycrystalline microstructures are inherently stochastic in nature.

An alternate class of schemes have been developed in the recent years that allow representation of microstructure using probabilistic descriptors. The approach is illustrated in Fig. 1 where a microstructural descriptor is evolved during processing rather than the actual microstructure itself. The simplest of these descriptors is the one-point probability measure, the orientation distribution function ($\mathcal{A}(\boldsymbol{g})$), which quantifies the volume fractions of crystals in the orientation space ($\boldsymbol{g}$). Under an applied deformation, texturing is simulated by numerically evolving the ODF using conservation laws (Clement, 1982). Conventional solution schemes are based upon representation of the ODF using a series of harmonics (Kocks et al., 2000;

* Corresponding author. Tel.: +1 734 615 7242.
E-mail address: veeras@umich.edu (V. Sundararaghavan).

0749-6419/$ - see front matter © 2011 Elsevier Ltd. All rights reserved.
doi:10.1016/j.ijplas.2011.09.001

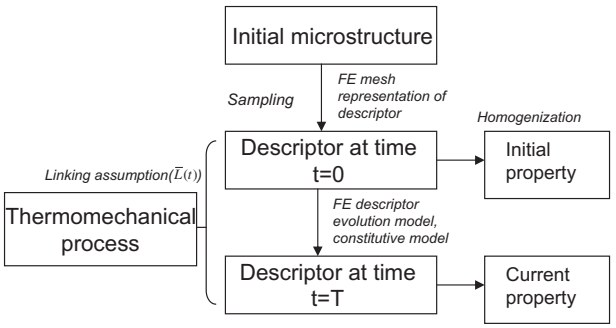

Fig. 1. Multiscale modeling using descriptors: the initial microstructure is sampled to obtain the descriptor which is then represented in a finite element mesh. The descriptors are directly evolved during thermomechanical processing to compute change in properties.

Bunge, 1982; Adams et al., 1992; Kalidindi and Duvvuru, 2005) or finite elements (Kumar and Dawson, 1996a,b). Since ODF representation does not contain information about the local neighborhood of crystals, Taylor assumption (Taylor, 1938) is typically used where all crystals are subject to the same deformation and equilibrium across grain boundaries is not captured.

In this paper, we investigate the use of finite element methods to evolve a higher order probability descriptor. Of specific interest is the two-point correlation function that arises in known expressions for mechanical and transport properties (Torquato, 2002; Beran et al., 1996) and correlates with defect-sensitive properties such as stress corrosion cracking and creep (Was et al., 1998). The two-point orientation correlation function (OCF), $\mathcal{F}(\boldsymbol{g}', \boldsymbol{g}, \boldsymbol{r})$, gives the probability density of finding orientations $\boldsymbol{g}'$ and $\boldsymbol{g}$ at the end points of a randomly placed vector $\boldsymbol{r}$ within the microstructure. In addition to containing volume fraction information, the OCF also contains crystal neighborhood information that can be used in models that predict interactions between grains.

Finite element representation of the two-point measure is challenging due to its high dimensionality, for example, nine-dimensional elements are needed to fully discretize the OCF for a 3D FCC polycrystal. Analytical approximations in the form of exponentially decaying functions (based on the Corson's model, Corson (1976), and Garmestani et al. (2001)) have been developed for approximating the two-point probability function. More recently, Adams exploited the use of intermediate representation called 'texture functions', approximated in Fourier space (Adams et al., 2005). However, these are global approximations and are not efficient in capturing sharp changes in the two-point probability function that occur in real microstructures. In this work, we attempt to develop a simplified finite element representation of the two-point measure using an approach analogous to 'separation of variables' method used for solving differential equations. Here, the OCF is described using interconnected layers of meshes in $\boldsymbol{g}$, $\boldsymbol{r}$ and $\boldsymbol{g}'$ spaces. The conditional orientation correlation function (COCF), $\mathcal{F}(\boldsymbol{g}'|(\boldsymbol{g},\boldsymbol{r}))$ is described using a finite element mesh in the 3D orientation space of $\boldsymbol{g}'$. This mesh is linked to a node $\boldsymbol{r}$ in a separate mesh representing the local neighborhood of orientation $\boldsymbol{g}$. As the microstructure evolves, the crystal reorientations close to an orientation ($\boldsymbol{g}$) is captured by updating probability fields in these interconnected finite element meshes. A novel total Lagrangian approach has been developed that allows evolution of probability densities while satisfying basic normalization constraints. The piecewise polynomial functions used to represent the COCF allow ease of construction of various orientation transformations, such as differencing, interpolation and projection. The improvement in prediction of texture and strains achieved by the COCF approach over ODF-based methods has been quantified through simple deformation analysis of a planar polycrystalline microstructure. For this simulation, we employ a viscoplastic (non-hardening) constitutive model and a Green's function based first order correction to the Taylor model previously developed in Adams et al. (1989).

2. Representation of the conditional orientation correlation function

The N-point correlation measure can be interpreted as the probability of finding the N vertices of a polyhedron separated by relative distances $x_1, x_2, \ldots, x_N$ in crystal orientations $\boldsymbol{g}_1, \boldsymbol{g}_2, \ldots, \boldsymbol{g}_N$ when tossed in the microstructure. The conditional orientation correlation function used in this work, $\mathcal{F}(\boldsymbol{g}'|(\boldsymbol{g},\boldsymbol{r}))$, is related to the two-point descriptor ($N = 2$). The function, hereafter simply called COCF, gives the probability density of occurrence of an orientation $\boldsymbol{g}'$ at the end point of a vector $\boldsymbol{r}$ (with length r) emanating from a given orientation $\boldsymbol{g}$ (Fig. 2). The function satisfies the following conservation equations at all times during deformation:

$$\int \mathcal{F}(\boldsymbol{g}'|(\boldsymbol{g},\boldsymbol{r}))d\boldsymbol{g}' = 1 \tag{1}$$

$$\int \mathcal{F}(\boldsymbol{g}'|(\boldsymbol{g},\boldsymbol{r}))\mathcal{P}(\boldsymbol{r}|\boldsymbol{g})d\boldsymbol{r} = \mathcal{A}(\boldsymbol{g}') \tag{2}$$

$$\int \mathcal{A}(\boldsymbol{g}')d\boldsymbol{g}' = 1 \tag{3}$$

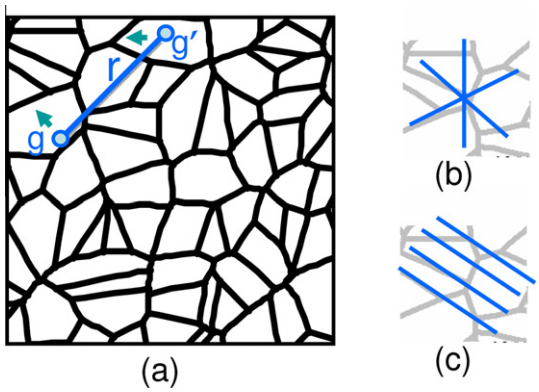

Fig. 2. (a) COCF ($\mathcal{F}(\boldsymbol{g}'|(\boldsymbol{g},\boldsymbol{r}))$) gives the probability density of occurrence of an orientation $\boldsymbol{g}'$ at the end point of a vector $\boldsymbol{r}$ emanating from orientation g. (b) Sampling along all directions results in a rotationally invariant OCF with scalar r. (c) Direction sensitive sampling for a vector representation of $\boldsymbol{r}$.

$$\int \mathcal{P}(\boldsymbol{r}|\boldsymbol{g})d\boldsymbol{r} = 1 \tag{4}$$

In the above equation $\mathcal{A}(\boldsymbol{g}')$ refers to the orientation distribution function (ODF) and $\mathcal{P}(\boldsymbol{r}|\boldsymbol{g})$ gives the probability density of occurrence of vector $\boldsymbol{r}$ from a location with orientation $\boldsymbol{g}$. $\mathcal{P}(\boldsymbol{r}|\boldsymbol{g})$ is a geometrical probability distribution that accounts for the finite size of the microstructure. In the derivation of Eq. (2), orientations $\boldsymbol{g}'$ and $\boldsymbol{g}$ are considered mutually independent variables, with the joint probability $\mathcal{G}(\boldsymbol{g}',\boldsymbol{g}) = \mathcal{A}(\boldsymbol{g})\mathcal{A}(\boldsymbol{g}')$.

In addition, the following constraints have to be satisfied by the COCF at all times:

$$\mathcal{F}(\boldsymbol{g}'|(\boldsymbol{g},r=0)) = \delta(\boldsymbol{g}-\boldsymbol{g}') \tag{5}$$

$$\mathcal{F}(\boldsymbol{g}'|(\boldsymbol{g},\boldsymbol{r})) \geqslant 0 \text{ (with } \mathcal{P}(\boldsymbol{r}|\boldsymbol{g}) \geqslant 0, \mathcal{A}(\boldsymbol{g}') \geqslant 0) \tag{6}$$

Here, δ stands for the dirac delta function. The distance r can be considered a scalar (using the notion of rotational invariance). Note that the correlation functions may also depend on the direction of r, in which case, parameter r must be considered as a vector. Use of scalar r simplifies the computational cost but captures less information about the polycrystal. We will discuss both cases in this work. In addition to the above constraints, the orientation space corresponding to all possible $\boldsymbol{g}$'s must satisfy the crystallographic symmetries of the chosen system (FCC, HCP, etc.) and the switching symmetry of the two-point measure.

Previously, analytical approximations (Garmestani et al., 2001) have been used to represent *discrete* two-point probability functions. For example, exponential functions in the following form can be used to represent the conditional two-point probability function for a discrete set of orientations $\boldsymbol{g}$:

$$P(g_j|(g_i,r)) = \begin{cases} V_j + (1-V_j)exp(-c_{ij}r^{n_{ij}}) & \text{if } i=j \\ V_j - V_j exp(-c_{ij}r^{n_{ij}}) & \text{if } i\neq j \end{cases} \tag{7}$$

where V_j is the volume fraction of grains with orientations $\boldsymbol{g}_j$. The parameters c_{ij} and n_{ij} are obtained by curve fitting the measured initial COCF. The above relationship is a smooth global approximation and is not efficient in capturing localized changes (at different $\boldsymbol{r}$) in the two-point probability function that occur in real microstructures. In this paper, we develop a new finite element discretization approach for representing the orientation correlation function. In this section, we first explain the representation scheme for the COCF using a *continuous* domain of orientations $\boldsymbol{g}$, i.e., the orientation space.

The complete orientation space of a polycrystal can be reduced to a smaller subset, called the fundamental region, as a consequence of crystal symmetries. Within the fundamental region, each crystal orientation is represented uniquely by a coordinate $\boldsymbol{g}$, the parametrization for the rotation (e.g. Euler angles, Rodrigues vector etc.). The ODF, represented by $\mathcal{A}(\boldsymbol{g})$, describes the local density of crystals over the fundamental region of orientation space. Consider a region R_δ which is a ball of radius δ centered at orientation $\boldsymbol{g}$ in the fundamental region. Let $v_f(R_\delta)$ be the volume fraction of crystals that have orientations that occur within volume R_δ. Assuming that the ODF is a continuous function in the fundamental region, the ODF at an orientation $\boldsymbol{g}$ is defined as:

$$\mathcal{A}(\boldsymbol{g}) = \lim_{\delta\to 0} \frac{v_f(R_\delta)}{\int_{R_\delta} d\boldsymbol{g}} \tag{8}$$

A variety of ODF representation techniques have been developed in literature, including spectral expansions and finite element representations. We employ the finite element approach where the ODF is represented through the nodal values of a finite element grid in the fundamental region (e.g. $\boldsymbol{g}$-mesh in Fig. 3).

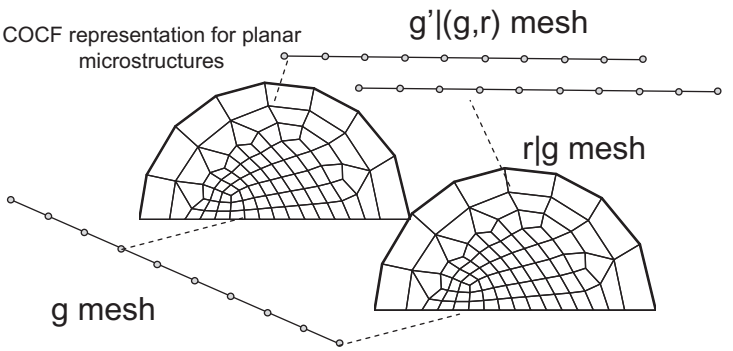

Fig. 3. COCF mesh representation for a planar microstructure (with fundamental region being a line between $-\pi/2$ to $\pi/2$). The $\boldsymbol{r}$ mesh is a semicircle with each node point giving the distance and orientation of a vector $\boldsymbol{r}$ drawn from orientation $\boldsymbol{g}$. Orientation $\boldsymbol{g}'$ located at the end of vector $\boldsymbol{r}$ is represented using a fundamental region connected to each node in the $\boldsymbol{r}$ mesh.

The COCF, $\mathcal{F}(\boldsymbol{g}'|(\boldsymbol{g},r))$, is represented in the FE discretized fundamental region (called mesh $M_{g'|gr}$). Another mesh (mesh $M_{r|g}$) in real space is considered that contains all possible distances (r) from an orientation $\boldsymbol{g}$. This is a 1D mesh if only scalar magnitudes of r is considered and a nD mesh in a general case if n-dimensional ($n = 2, 3$) vector locations $\boldsymbol{r}$ are considered. The mesh $M_{g'|gr}$ is represented at every node point in mesh $M_{r|g}$. The mesh $M_{r|g}$ is, in turn, defined for every node point in another FE discretized fundamental region (mesh M_g). The approach is illustrated in Fig. 3 for a planar microstructure (with fundamental region for $\boldsymbol{g}$ being a line between $-\pi/2$ to $\pi/2$). The approach used here allows easy visualization and interpretation of COCF evolution during deformation.

3. Probability update in finite element spaces

The probabilities are evolved from time $t = 0$ from an initial COCF that satisfies the conservation Eqs. (1)–(4). The initial orientation $\boldsymbol{g}_o$ of a crystal reorients during deformation and maps to a new orientation $\boldsymbol{g}_t$ at time t. Simultaneously, the finite element mesh of fundamental region M_g deforms with nodes located at $\boldsymbol{g}_o$ moving to new locations $\boldsymbol{g}_t$. We assume that the mapping from $\boldsymbol{g}_o$ to $\boldsymbol{g}_t$ is invertible.

The ODF $\mathcal{A}(\boldsymbol{g}_t)$ represents the volume density of crystals with orientation $\boldsymbol{g}_t$ at time t. The evolution of ODF is given by the conservation equation (3) as:

$$\int \mathcal{A}(\boldsymbol{g}_o, t=0) d\boldsymbol{g}_o = \int \mathcal{A}(\boldsymbol{g}_t) d\boldsymbol{g}_t = 1 \tag{9}$$

where $d\boldsymbol{g}_o$ represents the volume element in the undeformed (initial) ODF mesh (M_{g_o}) which becomes volume element $d\boldsymbol{g}_t$ at time t. A Jacobian $J(\boldsymbol{g}_o,t) = \det(\boldsymbol{F})$ gives the ratio of elemental volumes, where $\boldsymbol{F}$ is the reorientation gradient given as $\boldsymbol{F}(\boldsymbol{g}_o, t) = \frac{\partial \boldsymbol{g}_t}{\partial \boldsymbol{g}_o}$. Using the Jacobian, a map of the current mesh (at time t) to the reference mesh (at $t = 0$) can be made:

$$\int (\mathcal{A}(\boldsymbol{g}_o, t=0) - \hat{\mathcal{A}}(\boldsymbol{g}_o, t) J(\boldsymbol{g}_o, t)) d\boldsymbol{g}_o = 0 \tag{10}$$

The quantity written as $\hat{\mathcal{A}}(\boldsymbol{g}_o, t)$ is the volume density $\mathcal{A}(\boldsymbol{g}_t)$ plotted over the corresponding orientation ($\boldsymbol{g}_o$) in the initial mesh. Thus, $\hat{\mathcal{A}}(\boldsymbol{g}_o, t)$ gives the Lagrangian representation of the current ODF in the initial mesh M_{g_o}. If the integrand is continuous, a localized relationship of the following form can be used to update the ODF at any time t:

$$\hat{\mathcal{A}}(\boldsymbol{g}_o, t) J(\boldsymbol{g}_o, t) = \mathcal{A}(\boldsymbol{g}_o, t=0) \tag{11}$$

For computing $\boldsymbol{g}_t$, a reorientation velocity (computed from the constitutive model) $\boldsymbol{v} = \frac{\partial \boldsymbol{g}_t}{\partial t}$ is used. The reorientation velocity is computed at each nodal point in the mesh and the change in orientation $\Delta \boldsymbol{g}' = \boldsymbol{g}'_t - \boldsymbol{g}'_o$ is then stored at the nodal points in the fundamental region. Fig. 4 gives an idea of how the approach works for a one-dimensional fundamental region that is represented using two-noded finite elements with linear interpolation. Here, the Jacobian is simply the ratio of element lengths, i.e. current length divided by the initial length. If the element length decreases over time, the probability density has to increase based on Eq. (11) to maintain normalization of the ODF.

Note that the integrand in Eq. (10) needs to be continuous for the localization relationship to be valid. Thus, it is implied that $J(\boldsymbol{g}_o,t)$ needs to be continuous and consequently, $\boldsymbol{v}$ needs to be continuously differentiable (at least piecewise) in the fundamental region. The latter is rather a restriction on the constitutive model and macro–micro linking assumption that is used to compute $\boldsymbol{v}$.[1] Note that the differentiability of $\boldsymbol{v}$ will also ensure invertibility of the map from $\boldsymbol{g}_o$ to $\boldsymbol{g}_t$.

[1] Some rate-independent crystal plasticity models give sharp differences in reorientation velocities for orientations that are, in fact, very close to each other. When using such models, the Jacobian may become ill-defined.

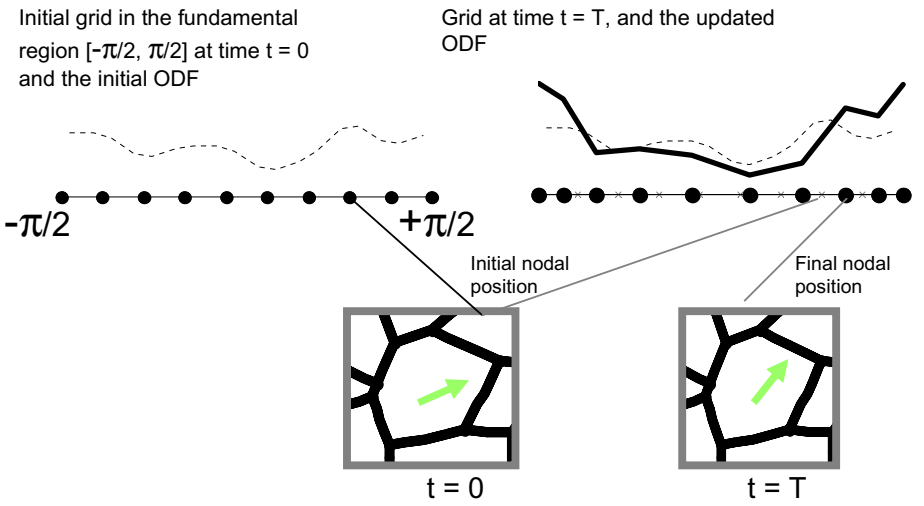

Fig. 4. Probability update scheme in FE space: during deformation, the nodal points ($\boldsymbol{g}$) of the FE mesh are moved to reflect reorientation ($\Delta\boldsymbol{g}$) of crystals. The new ODF is obtained using Eq. (11) that ensures that the normalization constraint (Eq. (9)) is met in the reoriented mesh.

Similar approach is used to update the probability densities $\mathcal{P}$ and $\mathcal{F}$ in the meshes $M_{r|g}$ and $M_{g'|gr}$, respectively. The evolution of geometrical probability density $\mathcal{P}$ is given by conservation equation (4) as:

$$\int (\widehat{\mathcal{P}}(\boldsymbol{r}_o, t|\boldsymbol{g}_t) J(\boldsymbol{r}_o, t|\boldsymbol{g}_t) - \mathcal{P}(\boldsymbol{r}_o, t=0|\boldsymbol{g}_t)) d\boldsymbol{r}_{o_g} = 0 \tag{12}$$

where $d\boldsymbol{r}_{o_g}$ represents the volume element in the undeformed (initial) mesh ($M_{r|g}$) and $J(\boldsymbol{r}_o, t|\boldsymbol{g}_t) = \det\left(\frac{\partial \boldsymbol{r}_L}{\partial \boldsymbol{r}_o}(\boldsymbol{g}_t)\right)$ is the Jacobian for a volume element initially at location $\boldsymbol{r}_o$ from orientation $\boldsymbol{g}_t$. A localized relation of the following form is used to compute the geometrical probability density at time t:

$$\widehat{\mathcal{P}}(\boldsymbol{r}_o, t|\boldsymbol{g}_t) J(\boldsymbol{r}_o, t|\boldsymbol{g}_t) = \mathcal{P}(\boldsymbol{r}_o, t=0|\boldsymbol{g}_t) \tag{13}$$

We consider the microstructure to be periodic, in which case, the initial probability $\mathcal{P}(\boldsymbol{r}_o, t=0|\boldsymbol{g}) = c_o$, a constant independent of $\boldsymbol{g}$. That is, from a given crystal, all r-vectors are equally probable due to periodicity.

For computing the COCF, we first look at the r-interdependence Eq. (2):

$$\int \mathcal{F}(\boldsymbol{g}'_t|(\boldsymbol{g}_t, \boldsymbol{r}_t)) \mathcal{P}(\boldsymbol{r}_t|\boldsymbol{g}_t) d\boldsymbol{r}_t = A(\boldsymbol{g}'_t) \tag{14}$$

The two localization relations given by Eqs. (11) and (13) are used to reduce the above equation:

$$\int \widehat{\mathcal{F}}(\boldsymbol{g}'_t|(\boldsymbol{g}_t, \boldsymbol{r}_o, t)) \frac{\mathcal{P}(\boldsymbol{r}_o, t=0|\boldsymbol{g}_t)}{J(\boldsymbol{r}_o, t|\boldsymbol{g}_t)} J(\boldsymbol{r}_o, t) d\boldsymbol{r}_o = \frac{\mathcal{A}(\boldsymbol{g}'_o, t=0)}{J(\boldsymbol{g}'_o, t)} \tag{15}$$

$$= \frac{1}{J(\boldsymbol{g}'_o, t)} \int \mathcal{F}(\boldsymbol{g}'_o, t=0|(\boldsymbol{g}_o, \boldsymbol{r}_o)) \mathcal{P}(\boldsymbol{r}_o, t=0|\boldsymbol{g}_o) d\boldsymbol{r}_o \tag{16}$$

$$\int c_o (\widehat{\mathcal{F}}(\boldsymbol{g}'_t|(\boldsymbol{g}_t, \boldsymbol{r}_o, t)) \frac{J(\boldsymbol{g}'_o, t) J(\boldsymbol{r}_o, t)}{J(\boldsymbol{r}_o, t|\boldsymbol{g}_t)} - \mathcal{F}(\boldsymbol{g}'_o, t=0|(\boldsymbol{g}_o, \boldsymbol{r}_o))) d\boldsymbol{r}_o = 0 \tag{17}$$

In the above derivation, we have used the fact that $\mathcal{P}(\boldsymbol{r}_o, t=0|\boldsymbol{g}) = c_o$ at time $t = 0$ due to periodicity. The localization relationship obtained from Eq. (17) leads to a simple probability update strategy for the COCF:

$$\widehat{\mathcal{F}}(\boldsymbol{g}'_t|(\boldsymbol{g}_t, \boldsymbol{r}_o, t)) \frac{J(\boldsymbol{g}'_o, t) J(\boldsymbol{r}_o, t)}{J(\boldsymbol{r}_o, t|\boldsymbol{g}_t)} = \mathcal{F}(\boldsymbol{g}'_o, t=0|(\boldsymbol{g}_o, \boldsymbol{r}_o)) \tag{18}$$

The above equation gives the COCF in locations ($\boldsymbol{g}_t$, $\boldsymbol{r}_t$) for all times $t > 0$. Finally, we need to develop a mesh update strategy that ensures the normalization equation for COCF ($\mathcal{F}$) Eq. (1) is satisfied at times $t > 0$:

$$\int \mathcal{F}(\boldsymbol{g}'_t|(\boldsymbol{r}_t, \boldsymbol{g}_t)) d\boldsymbol{g}'_{t_{rg}} = 1 \tag{19}$$

where $d\boldsymbol{g}'_{t_{rg}}$ represents the volume element at orientation $\boldsymbol{g}'_t$ in the deformed COCF mesh ($M_{g'|gr}$) located at a distance of $\boldsymbol{r}_t$ from $\boldsymbol{g}_t$.

Using Eq. (18), the conservation equation is written as:

$$\int \mathcal{F}(\mathbf{g}'_o, t=0|(\mathbf{g}_o,\mathbf{r}_o))\frac{J(\mathbf{r}_o,t|\mathbf{g}_t)}{J(\mathbf{g}'_o,t)J(\mathbf{r}_o,t)}d\mathbf{g}'_{t_{rg}} = \int \mathcal{F}(\mathbf{g}'_o, t=0|(\mathbf{g}_o,\mathbf{r}_o))d\mathbf{g}'_{o_{rg}} = 1 \tag{20}$$

By inspection of the above equation, the Jacobian for the COCF mesh evolution can be obtained as:

$$J(\mathbf{g}'_o,t|(\mathbf{r}_t,\mathbf{g}_t)) = \det\left(\frac{\partial \mathbf{g}'_t}{\partial \mathbf{g}'_o}(\mathbf{r}_t,\mathbf{g}_t)\right) = \frac{J(\mathbf{g}'_o,t)J(\mathbf{r}_o,t)}{J(\mathbf{r}_o,t|\mathbf{g}_t)} \tag{21}$$

The initial COCF mesh (at $t = 0$) is the same at all locations $\mathbf{r}$ and $J(\mathbf{g}'_o,t|(\mathbf{r}_o,\mathbf{g}_t))$ is also numerically equal to the above Jacobian. This equation gives a mesh update strategy for the COCF. As explained previously, ODF mesh update uses the reorientation gradient $\mathbf{F}(\mathbf{g}'_o,t) = \frac{\partial \mathbf{g}_t}{\partial \mathbf{g}_o}$ computed from the reorientation velocity $\boldsymbol{v} = \frac{\partial \mathbf{g}_t}{\partial t}$ (as given by the constitutive model). At each location $\mathbf{r}_t$ and $\mathbf{g}$, the node points of the COCF mesh ($M_{g'|gr}$) are moved using the same reorientation gradient (with Jacobian $J(\mathbf{g}'_o,t)$) but scaled by a factor $\left(\frac{J(\mathbf{r}_o,t)}{J(\mathbf{r}_o,t|\mathbf{g}_t)}\right)^{\frac{1}{d}}$, where d is the dimensionality of the orientation space. We next look at the approach to compute this scaling factor.

Apart from crystal reorientations, the COCF also evolves due to stretching of grains during deformation (Fig. 5). Let us say, for now, that the velocity gradient ($\mathbf{L}$) for each grain of orientation $\mathbf{g}$ can be computed (this is discussed later in Section 4.1). In Fig. 5, the rate of change of vector $\mathbf{r}$ originating from orientation $\mathbf{g}$ (shown as a red line) can be found by integrating $\mathbf{L}d\mathbf{r}$ over the vector $\mathbf{r}$. However, in the COCF approach, the velocity gradient $\mathbf{L}$ along the vector $\mathbf{r}$ is only known in a statistical sense. For e.g. the average velocity gradient at a distance of $\mathbf{r}'(\mathbf{r}' = \lambda\mathbf{r},\ 0 \leqslant \lambda \leqslant 1)$ from orientation $\mathbf{g}$, denoted as $\langle \mathbf{L}(\mathbf{r}'|\mathbf{g})\rangle$, can be found by averaging over the COCF:

$$\langle \mathbf{L}(\mathbf{r}'|\mathbf{g})\rangle = \int \mathcal{F}(\mathbf{g}'|(\mathbf{g},\mathbf{r}'))L(\mathbf{g}')d\mathbf{g}'_{r'g} \tag{22}$$

The average rate of change of vector $\mathbf{r}$ can then be written as a path integral of averaged velocity gradient ($\langle \mathbf{L}(\mathbf{r}'|\mathbf{g})\rangle$) along $\mathbf{r}$:

$$\langle \dot{\mathbf{r}}\rangle_{\mathbf{g}} = \int_0^{\mathbf{r}} \langle \mathbf{L}(\mathbf{r}'|\mathbf{g})\rangle d\mathbf{r}'_g \tag{23}$$

Nodes in the mesh $M_{r|g}$ are updated using the velocities computed in Eq. (23) from which the Jacobian $J(\mathbf{r}_o,t|\mathbf{g})$ can be computed. The probability $\mathcal{P}(\mathbf{r}_t)$ is computed from the relationship:

$$\int \mathcal{P}(\mathbf{r}_t|\mathbf{g}_t)\mathcal{A}(\mathbf{g}_t)d\mathbf{g}_t = \mathcal{P}(\mathbf{r}_t) \tag{24}$$

Then, the Jacobian is computed as $J(\mathbf{r}_o,t) = \frac{\mathcal{P}(\mathbf{r}_o)}{\mathcal{P}(\mathbf{r}_t)}$.

3.1. Case of rotationally invariant COCF

When using the *rotationally invariant* COCF, only the rate of change of *magnitude* of $\mathbf{r}$ needs to be calculated. The vector $\mathbf{r}'$ is written as a product of the magnitude r' and a unit vector $\mathbf{n}$ (i.e. $\mathbf{r}' = r'\mathbf{n}$). Eq. (23) is rewritten in terms of the stretch rate

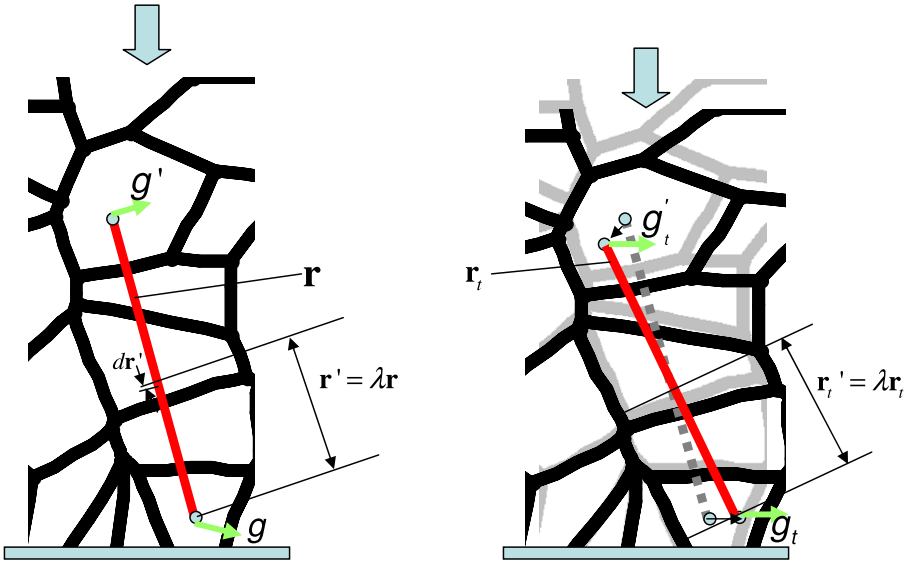

Fig. 5. During deformation, the two-point descriptor evolves due to reorientation of crystals with initial orientation $\mathbf{g}'$ and $\mathbf{g}$ at the end points of vector $\mathbf{r}$. In addition, both the length and orientation of $\mathbf{r}$ vector changes during deformation.

tensor $\langle \boldsymbol{D} \rangle$ (symmetric part of $\langle \boldsymbol{L} \rangle$) and another integral is performed over the surface of a unit sphere in order to average over all possible unit vectors $\boldsymbol{n}$.

$$\langle \dot{r} \rangle_{\boldsymbol{g}} = \int \left[\int_0^r \boldsymbol{n}^T \langle \boldsymbol{D}(\boldsymbol{n}r' | \boldsymbol{g}) \rangle \boldsymbol{n} dr'_g \right] d\boldsymbol{n} \tag{25}$$

The average velocity gradient is computed from the rotationally invariant COCF as follows:

$$\langle \boldsymbol{L}(\boldsymbol{n}r' | \boldsymbol{g}) \rangle = \int \mathcal{F}(\boldsymbol{g}' | (\boldsymbol{g}, r')) L(\boldsymbol{g}') d\boldsymbol{g}'_{r'g} \tag{26}$$

The right hand side of the above expression is clearly independent of $\boldsymbol{n}$ due to the use of rotationally invariant COCF (i.e. $\langle \boldsymbol{L}(\boldsymbol{n}\ r' | \boldsymbol{g}) \rangle = \langle \boldsymbol{L}(r' | g) \rangle$). Thus, Eq. (25) can be rewritten as follows:

$$\langle \dot{r} \rangle_{\boldsymbol{g}} = \left[\int_0^r \langle \boldsymbol{D}(r' | \boldsymbol{g}) \rangle dr'_g \right] \left[\int \boldsymbol{n}^T \boldsymbol{n} d\boldsymbol{n} \right] \tag{27}$$

Using the property $\int \boldsymbol{n}^T \boldsymbol{n} d\boldsymbol{n} = \frac{1}{3} \delta_{ij}$, we can rewrite Eq. (27) as:

$$\langle \dot{r} \rangle_{\boldsymbol{g}} = \frac{1}{3} \int_0^r trace(\langle \boldsymbol{D}(r' | \boldsymbol{g}) \rangle) dr'_g \tag{28}$$

Note that the velocity $\langle \dot{r} \rangle_{\boldsymbol{g}}$ will be zero in viscoplastic analysis due to the incompressibility constraint $trace(\langle \boldsymbol{D} \rangle) = 0$.

Remark 1. Note that the rate of change of r-vector between two orientations (g and g') can be accurately computed if conditional three-point probability functions are known (Adams et al., 1989):

$$\langle \boldsymbol{L}(\boldsymbol{r}' | (\boldsymbol{g}', \boldsymbol{g}, \boldsymbol{r})) \rangle = \int \mathcal{F}(\boldsymbol{g}'' | (\boldsymbol{g}', \boldsymbol{g}, \boldsymbol{r}, \boldsymbol{r}')) L(\boldsymbol{g}'') d\boldsymbol{g}''_{g'gr'r} \tag{29}$$

$$\langle \dot{\boldsymbol{r}} \rangle_{(\boldsymbol{g}, \boldsymbol{g}')} = \int_0^{\boldsymbol{r}} \langle \boldsymbol{L}(\boldsymbol{r}' | (\boldsymbol{g}', \boldsymbol{g}, \boldsymbol{r})) \rangle d\boldsymbol{r}'_{g'gr} \tag{30}$$

where $\mathcal{F}(\boldsymbol{g}'' | (\boldsymbol{g}', \boldsymbol{g}, \boldsymbol{r}, \boldsymbol{r}'))$ is the probability of orientation g'' at a distance $r' = \lambda r$ from orientation g given that orientation g' is at a distance of r from g. Here, the rate of change $\langle \dot{\boldsymbol{r}} \rangle$ is assumed to depend on both g and g'. In the current work, we compute the rate of change $\langle \dot{\boldsymbol{r}} \rangle$ using only the starting orientation g. This is based on our Bayesian separation of variables: $\mathcal{F}(\boldsymbol{g}, \boldsymbol{g}', \boldsymbol{r}) = \mathcal{F}(\boldsymbol{g}' | (\boldsymbol{g}, \boldsymbol{r})) \mathcal{P}(\boldsymbol{r} | \boldsymbol{g}) \mathcal{A}(\boldsymbol{g})$. In the second term ($\mathcal{P}(\boldsymbol{r} | \boldsymbol{g})$), the deformation of r-mesh is modeled to depend only on the starting orientation g. Our motivation here was to restrict ourselves to the known two-point probability function and avoid computing or storing the even more complex three-point probability function. In another paper (Garmestani et al., 2001), the three-point probability function was approximated using the known two-point probability functions, but the approximation violated the normalization relationships for the three-point probability function. Derivation of consistent approximations are the subject of recent research (Mikdam et al., 2009).

3.2. Symmetry constraints in the COCF

Since $\boldsymbol{g}$ and $\boldsymbol{g}'$ can be switched in the joint distribution ($\mathcal{F}(\boldsymbol{g}, \boldsymbol{g}', \boldsymbol{r})$) without change in the probability density, a symmetry relationship of the following form is obtained:

$$\mathcal{F}(\boldsymbol{g} | (\boldsymbol{g}', \boldsymbol{r})) \mathcal{P}(\boldsymbol{r} | \boldsymbol{g}') \mathcal{A}(\boldsymbol{g}') = \mathcal{F}(\boldsymbol{g}' | (\boldsymbol{g}, \boldsymbol{r})) \mathcal{P}(\boldsymbol{r} | \boldsymbol{g}) \mathcal{A}(\boldsymbol{g}) \tag{31}$$

Substituting the localized Lagrangian conservation relationships in the above relationship leads to the following equation:

$$\frac{\mathcal{F}(\boldsymbol{g}_o, t = 0 | (\boldsymbol{g}'_o, \boldsymbol{r}_o))}{J(\boldsymbol{g}_o, t | (\boldsymbol{g}', \boldsymbol{r}))} \frac{\mathcal{P}(\boldsymbol{r}_o, t = 0 | \boldsymbol{g}')}{J(\boldsymbol{r}_o, t | \boldsymbol{g}')} \frac{\mathcal{A}(\boldsymbol{g}'_o)}{J(\boldsymbol{g}'_o, t)} = \frac{\mathcal{F}(\boldsymbol{g}'_o, t = 0 | (\boldsymbol{g}_o, \boldsymbol{r}_o))}{J(\boldsymbol{g}'_o, t | (\boldsymbol{g}, \boldsymbol{r}))} \frac{\mathcal{P}(\boldsymbol{r}_o, t = 0 | \boldsymbol{g})}{J(\boldsymbol{r}_o, t | \boldsymbol{g})} \frac{\mathcal{A}(\boldsymbol{g}_o)}{J(\boldsymbol{g}_o, t)} \tag{32}$$

Using the definition for Jacobian of COCF (Eq. (18)) and the fact that $\mathcal{P} = c_o$ at time $t = 0$, the above equation reduces to:

$$\mathcal{F}(\boldsymbol{g}_o, t = 0 | (\boldsymbol{g}'_o, \boldsymbol{r}_o)) \mathcal{A}(\boldsymbol{g}'_o) = \mathcal{F}(\boldsymbol{g}'_o, t = 0 | (\boldsymbol{g}_o, \boldsymbol{r}_o)) \mathcal{A}(\boldsymbol{g}_o) \tag{33}$$

Note that the reference COCF sampled from the microstructure satisfies the above constraint. This indicates that the evolution of the COCF will continue to follow the symmetry constraint Eq. (31) when using the proposed probability update scheme.

4. Constitutive modeling

The OCF evolution of a viscoplastic polycrystal is calculated using the following constitutive model (Asaro and Needleman, 1985). The velocity gradient of a crystal with orientation, $\boldsymbol{g}$ (and rotation matrix $\boldsymbol{R}$) is taken to be of the following form:

$$\boldsymbol{L}(\boldsymbol{g}) = \boldsymbol{\Omega} + \boldsymbol{R}\sum_{\alpha}\dot{\gamma}^{\alpha}\acute{\boldsymbol{S}}^{\alpha}\boldsymbol{R}^{T} \tag{34}$$

where $\boldsymbol{\Omega}$ is the lattice spin, $\dot{\gamma}^{\alpha}$ is the shearing rate along the slip system α and $\acute{\boldsymbol{S}}^{\alpha}$ is the Schmid tensor for the slip system α, given by $(\acute{\boldsymbol{m}}^{\alpha} \otimes \acute{\boldsymbol{n}}^{\alpha})$, where $\acute{\boldsymbol{m}}^{\alpha}$ is the slip direction and $\acute{\boldsymbol{n}}^{\alpha}$ is the slip plane normal, both in the crystal lattice frame. The expressions for the spin and symmetric parts are obtained as shown below:

$$\boldsymbol{\Omega} = \boldsymbol{W} - \boldsymbol{R}\sum_{\alpha}\dot{\gamma}^{\alpha}\acute{\boldsymbol{Q}}^{\alpha}\boldsymbol{R}^{T} \tag{35}$$

$$\acute{\boldsymbol{D}} = \sum_{\alpha}\dot{\gamma}^{\alpha}\acute{\boldsymbol{P}}^{\alpha} \tag{36}$$

where $\acute{\boldsymbol{P}}^{\alpha}$ and $\acute{\boldsymbol{Q}}^{\alpha}$ are the symmetric and skew parts of the Schmid tensor respectively and $\acute{\boldsymbol{D}}$ is the deviatoric deformation rate expressed in the lattice frame through, $\acute{\boldsymbol{D}} = \boldsymbol{R}^{T}\boldsymbol{D}\boldsymbol{R}$. The shearing rate on slip systems is given by a power law and we further assume that all slip systems have identical slip system resistance.

$$\dot{\gamma}^{\alpha} = \dot{\gamma}^{0}\left|\frac{\tau^{\alpha}}{s}\right|^{1/m} sign\left(\frac{\tau^{\alpha}}{s}\right) \tag{37}$$

where s is the slip system resistance, m is the strain rate sensitivity, $\dot{\gamma}^{0}$ is a reference rate of shearing and τ^{α} is the resolved shear stress on slip system α. Further, the resolved stress is related to the deviatoric crystal Cauchy stress as

$$\tau^{\alpha} = \acute{\boldsymbol{\sigma}} \cdot \acute{\boldsymbol{P}}^{\alpha} \tag{38}$$

If the velocity gradient for the crystal ($\boldsymbol{L}(\boldsymbol{g})$) is known, then solving the system of Eqs. (36)–(38) will lead to the deviatoric crystal cauchy stress ($\acute{\boldsymbol{\sigma}}$) and the shear rate ($\dot{\gamma}^{\alpha}$). A Newton algorithm is used to find the stress for a given velocity gradient and orientation. The secant moduli (symmetric tensor $\acute{\boldsymbol{N}}$) that relates the deviatoric deformation rate to the deviatoric stress tensor (as in $\acute{\boldsymbol{\sigma}} = \acute{\boldsymbol{N}}\acute{\boldsymbol{D}}$) in the lattice frame is then computed based on Eq. (39). The secant moduli in the lattice frame is then rotated back to the sample reference frame to calculate $\boldsymbol{N}$.

$$\acute{N}_{ijkl} = \left[\sum_{\alpha}\left(\frac{\dot{\gamma}_{o}}{s}\right)|\acute{P}^{\alpha}_{rs}\acute{\sigma}_{rs}/s|^{\frac{1}{m}-1}\acute{P}^{\alpha}_{ij}\acute{P}^{\alpha}_{kl}\right]^{-1} \tag{39}$$

4.1. Interaction law

In the following section, the interaction law is derived for a viscoplastic polycrystal following an integral equation approach (Molinari et al. (1987)). We denote by $\boldsymbol{T}$ the local Cauchy stress, $\boldsymbol{T} = \boldsymbol{\sigma} - p\boldsymbol{I}$, with $\boldsymbol{\sigma}$ representing the deviatoric cauchy stress, p representing the pressure and $\boldsymbol{I}$ being the second-order identity tensor. $\boldsymbol{N}$ refers to the secant modulus (in the sample reference frame) derived from the constitutive problem with the relationship $\boldsymbol{\sigma} = \boldsymbol{N}\boldsymbol{D} = \boldsymbol{N}\boldsymbol{L}$. Therefore, the governing equations for deformation (equilibrium equation with incompressibility constraint) in the polycrystal can be expressed as:

$$T_{ij,j} = (N_{ijkl}L_{kl})_{,j} - p_{,i} = 0 \quad \text{with} \quad L_{ii} = 0 \tag{40}$$

A macroscopic velocity gradient $\overline{\boldsymbol{L}}$ (with $\overline{L}_{ii} = 0$) is imposed upon the aggregate. Our objective is to find out the *local* velocity gradient ($\boldsymbol{L}$) in each crystal that satisfies the above governing equation. To this end, we first decompose $\boldsymbol{N}$ as the sum of a uniform part $\overline{\boldsymbol{N}}$ and a space dependent part $\tilde{\boldsymbol{N}}$ to obtain $\boldsymbol{N} = \overline{\boldsymbol{N}} + \tilde{\boldsymbol{N}}$. The uniform part is a tensor that is constant over the microstructure. In this work, the constant tensor $\overline{\boldsymbol{N}}$ is taken as the instantaneous secant moduli of the (first order) homogenized microstructure:

$$\overline{\boldsymbol{N}} = \int \mathcal{A}(\boldsymbol{g})\boldsymbol{N}(\overline{\boldsymbol{L}}, \boldsymbol{g})d\boldsymbol{g} \tag{41}$$

Molinari et al. (1987) proposed a Green's function solution for the set of PDEs represented by Eq. (40) and the compatibility conditions, $L_{ii} = 0$

$$L_{ik}(\boldsymbol{r}) = \overline{L}_{ik} + \int G_{ij,kl}(\boldsymbol{r} - \boldsymbol{r}')\tilde{\sigma}_{jl}(\boldsymbol{r}')d\boldsymbol{r}' \tag{42}$$

Here, $G_{ij,kl}$ is the spatial Green's function that is obtained from Eq. (40) (Fig. 6), the positions $\boldsymbol{r}$ are those computed at current time t and the fluctuation stress is given as:

$$\tilde{\sigma}_{jl}(\boldsymbol{r}') = \tilde{N}_{jlrs}(\boldsymbol{L}(\boldsymbol{r}'), \boldsymbol{g}(\boldsymbol{r}'))L_{rs}(\boldsymbol{r}') \tag{43}$$

Using an abbreviated form for the convolution operator, the above equation can be concisely written as:

$$\boldsymbol{L}(\boldsymbol{r}) = \overline{\boldsymbol{L}} + \boldsymbol{G}(\boldsymbol{r} - \boldsymbol{r}') * \tilde{\boldsymbol{\sigma}}(\boldsymbol{r}') \tag{44}$$

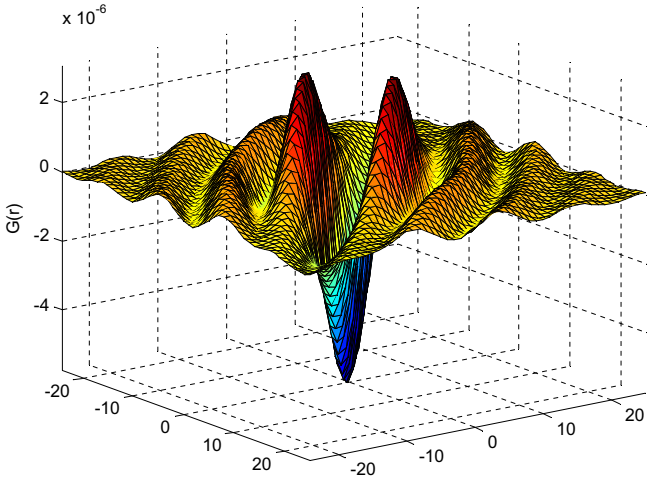

Fig. 6. Real part of Green's function operator $G_{11,11}(\boldsymbol{r})$ for a 2D microstructure. The function peaks at $\boldsymbol{r} = (0,0)$ and decays to zero at large $\boldsymbol{r}$.

Adams et al. (1989) developed an approach where statistical correlation functions can be used to compute this velocity gradient. When using the COCF descriptor, we assume that all grains with orientation $\boldsymbol{g}$ have one local velocity gradient that is calculated as an ensemble average. Note that there may be differences in the deformation of crystals with the same orientation but located at different positions in the microstructure. Unlike aggregate FE models, the local neighborhoods are not explicitly resolved in the COCF descriptor but are rather averaged for crystals with orientation $\boldsymbol{g}$. Symbol $\langle \cdot \rangle_{\boldsymbol{g}}$ denotes such an ensemble average. Applying this to Eq. (44), the ensemble average of the local velocity gradients belonging to the same orientation $\boldsymbol{g}^*$ can be calculated (approximation is valid within the ergodic hypothesis described in Beran (1968)):

$$\boldsymbol{L}(\boldsymbol{g}^*) = \langle \boldsymbol{L}(\boldsymbol{r}) \rangle_{\boldsymbol{g}(\boldsymbol{r})=\boldsymbol{g}^*} = \overline{\boldsymbol{L}} + \boldsymbol{G}(\boldsymbol{r}-\boldsymbol{r}') * \langle \tilde{\boldsymbol{\sigma}}(\boldsymbol{r}') \rangle_{\boldsymbol{g}(\boldsymbol{r})=\boldsymbol{g}^*} = \overline{\boldsymbol{L}} + \boldsymbol{G}(\boldsymbol{r}-\boldsymbol{r}') * \left[\int \mathcal{F}(\boldsymbol{g}'|(\boldsymbol{r}-\boldsymbol{r}', \boldsymbol{g}^*)) \tilde{\boldsymbol{\sigma}}(\boldsymbol{g}') d\boldsymbol{g}'_{r'g} \right] \tag{45}$$

This equation is non-linear since $\tilde{\boldsymbol{\sigma}}$ in itself depends on the velocity gradient (Eq. (43)). The velocity gradient for any orientation $\boldsymbol{g}$ can be found by solving the above equation in a self-consistent iterative manner. No such iterations are required if we use a simplifying assumption that velocity gradient field does not deviate too far from the uniform field of the Taylor-type polycrystal (using a first order correction $\boldsymbol{L}(\boldsymbol{r}') \approx \overline{\boldsymbol{L}}$):

$$\langle \tilde{\boldsymbol{\sigma}}(\boldsymbol{r}') \rangle_{\boldsymbol{g}(\boldsymbol{r})=\boldsymbol{g}^*} \approx \int \mathcal{F}(\boldsymbol{g}'|(\boldsymbol{r}-\boldsymbol{r}', \boldsymbol{g}^*)) \tilde{\boldsymbol{N}}(\overline{\boldsymbol{L}}, \boldsymbol{g}') \overline{\boldsymbol{L}} d\boldsymbol{g}'_{r'g} \tag{46}$$

For the purpose of demonstration of our probability update scheme, we employ this first order correction in a similar vein as Garmestani et al. (2001). The average velocity gradient provided by the approach is enough to compute the necessary Jacobians used in updating the probability functions. There is, however, further room for development of the Green's function approach. Extensions to the case where state variables (e.g. s in Eq. (37)) evolve with deformation has been treated in Kumar and Dawson (1996a) for ODFs. A similar approach may be used where ensemble average of the state variable is computed for all grains of the same orientation. In addition, Eq. (45) can be enhanced by modifying it to calculate the velocity gradient as a function of distance from orientation $\boldsymbol{g}$. These enhancements will be a subject of future study.

5. Numerical examples

The improvement in prediction of texture and strains achieved by the COCF approach over ODF-based methods has been quantified through simple deformation analysis of a planar polycrystalline microstructure. Orientations of planar crystals are characterized by the two dimensional rotation $\boldsymbol{R}$ relating the crystal lattice frame to the reference sample frame. A parametrization of the associated rotation group is,

$$\boldsymbol{R} = \boldsymbol{I} cos(\boldsymbol{r}) - \boldsymbol{E} sin(\boldsymbol{r}) \tag{47}$$

where $\boldsymbol{r}$ is the angle between the crystal and sample axes, $\boldsymbol{E}$ is the two dimensional alternator ($E_{11} = E_{22} = 0$, $E_{12} = -E_{21} = 1$), and $\boldsymbol{I}$ is the identity tensor. Under the symmetry, crystal orientations can be described uniquely by parameters drawn from a simply connected fundamental region $[a, a+\pi)$. Out of convenience, we will restrict the choice of fundamental regions to the interval closest to the origin $(-\pi/2, \pi/2)$. Due to symmetry, the orientation $\pi/2$ is exactly the same as orientation $-\pi/2$. This constraint on the ODF and COCF is enforced in practise by using periodic boundary conditions in the finite element mesh (Sundararaghavan and Zabaras, 2007) wherein node at $g = \pi/2$ is considered a dependent node with field values updated

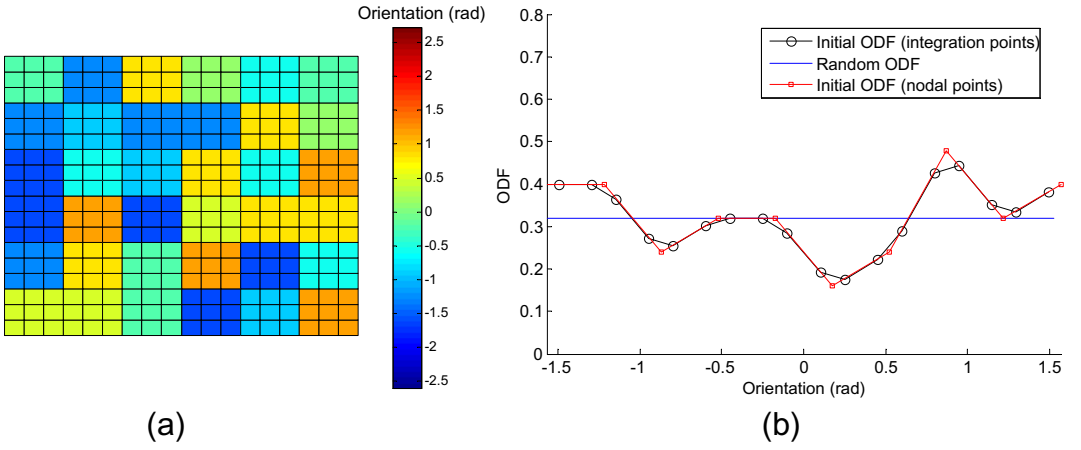

Fig. 7. (a) The initial (periodic) RVE with 324 elements and 36 crystals. Each crystal is divided into nine elements. (b) The initial ODF sampled from the RVE is plotted on a finite element grid in the fundamental region $(-\pi/2, \pi/2)$. Both locations of nodal points and integration points are indicated.

using the values at $g = -\pi/2$. The crystal reorientation velocity follows by taking a derivative of relation Eq. (47) and using Ω from Eq. (35):

$$\boldsymbol{v} = \frac{1}{2} E \cdot \Omega \tag{48}$$

The following parameters were used in the power law: $\dot{\gamma}^0 = 1\ \mathrm{s}^{-1}$, $s = 27.17$ MPa and $m = 0.05$. A specific crystal geometry with two slip systems at orientation $-\pi/6$ and $+\pi/6$ were considered. Kumar and Dawson (1996b) showed that this model leads to continuity in both reorientation velocity (v) and its gradient (∇v) over the orientation space. Thus, a localized Lagrangian model is admissible for the test case. The imposed macroscopic velocity gradient $\boldsymbol{L}$ (tension) is given as:

$$\boldsymbol{L} = \eta \begin{bmatrix} 1 & 0 \\ 0 & -1 \end{bmatrix} \tag{49}$$

Here η is a constant strain rate taken to be 0.1. To test the proposed formulation, a representative volume element (RVE) containing 36 crystals was chosen. The microstructure is divided into $N \times N$ ($N = 18$) smaller elements and the orientations were randomly assigned. It is assumed that this microstructure contains adequate number of grains to represent the overall one and two-point statistics. To avoid edge effects in sampling two-point statistics, it is assumed that the microstructure is periodic in the x-and y-directions. Fig. 7 shows the initial microstructure as well as the initial ODF sampled from the RVE. The initial ODF is plotted on a finite element grid with nine line elements in the fundamental region $(-\pi/2, \pi/2)$ of a planar microstructure. Both locations of nodal points and integration points are indicated in Fig. 7(b).

The COCF of the microstructure was sampled to compute probabilities at the node points of finite element meshes $M_{g'|gr}$, $M_{r|g}$ and M_g. Grains that have orientations close to the nodal points in the M_g mesh (within an error of $\pm\delta\boldsymbol{g}$,

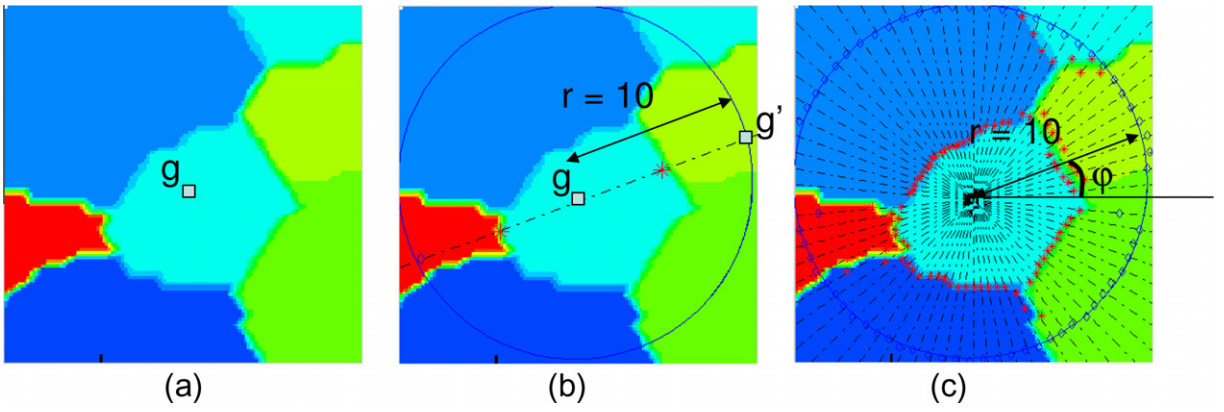

Fig. 8. Illustration of the sampling approach for COCF: (a) sample a pixel in a grain with orientation g corresponding to a node point in the M_g mesh, (b) draw a line passing through the pixel to identify the orientation g' at a distance r, increment the weights in a 3D array $F(g, r, g')$ and (c) sample lines at various angles to capture orientation dependence. The lengths and orientation of the lines are chosen based on the location of node points in the $M_{r|g}$ mesh.

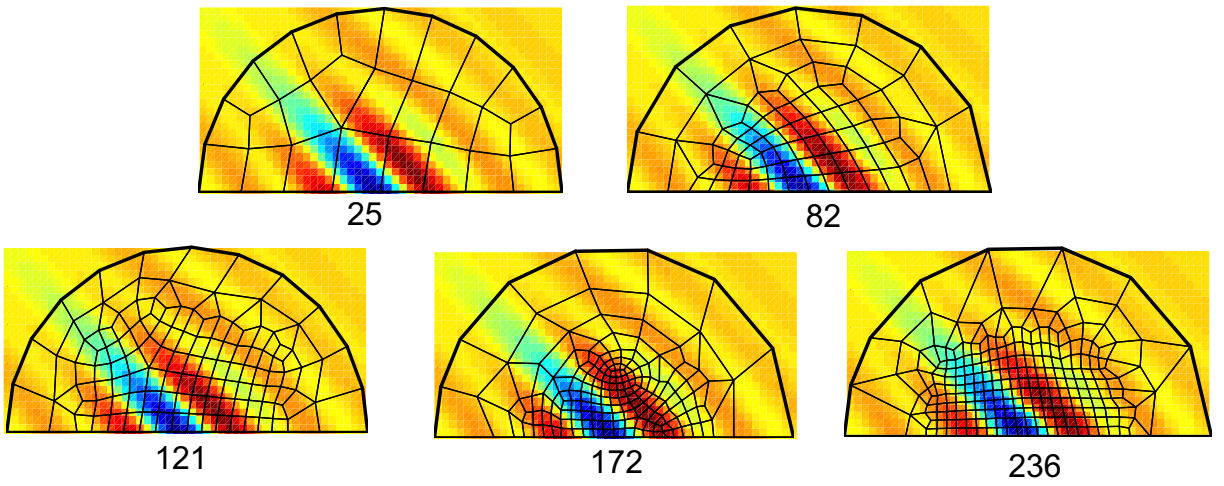

Fig. 9. Various meshes used to discretize the $\boldsymbol{r}$ space for testing the convergence of the Green's function approach. The Green's function $G_{11,11}$ is superposed on the r-mesh as a color contour.

$\delta\boldsymbol{g}$ = 0.05 rad being a small smoothing parameter in the g-space) are chosen for sampling. From these selected grains, a set of $\boldsymbol{r}$ vectors are drawn. The lengths and orientation of the $\boldsymbol{r}$ vectors are chosen based on the location of node points in the $M_{r|g}$ mesh. If the end point of these vectors fall in orientation that corresponds to a node point (within the smoothing parameter) in the COCF mesh $M_{g'|gr}$, then the weight for this node is incremented by one. The approach is illustrated in Fig. 8. COCF weights are computed for all combination of node points in meshes $M_{r|g}$ and M_g. The nodal probabilities are then computed through normalization of the weights over the COCF mesh ($M_{g'|gr}$). Note that there is no limitation on the number of crystals in the actual microstructure when using the COCF mesh. The COCF is sampled using a fixed set of elements in the $\boldsymbol{g}$, $\boldsymbol{r}$ and $\boldsymbol{g}'$ meshes irrespective of how many grains are actually present in the microstructure. The present example was only used as a simple test case and larger systems (with more grains) could have been considered without restriction.

The Green's function ($G_{11,11}$) for the proposed constitutive model parameters was shown in Fig. 6. From analysis of the decay of this and other components of the tensor ($G_{ij,kl}$), a cut-off distance of 25 mm was chosen for the $M_{r|g}$ mesh. The micro-

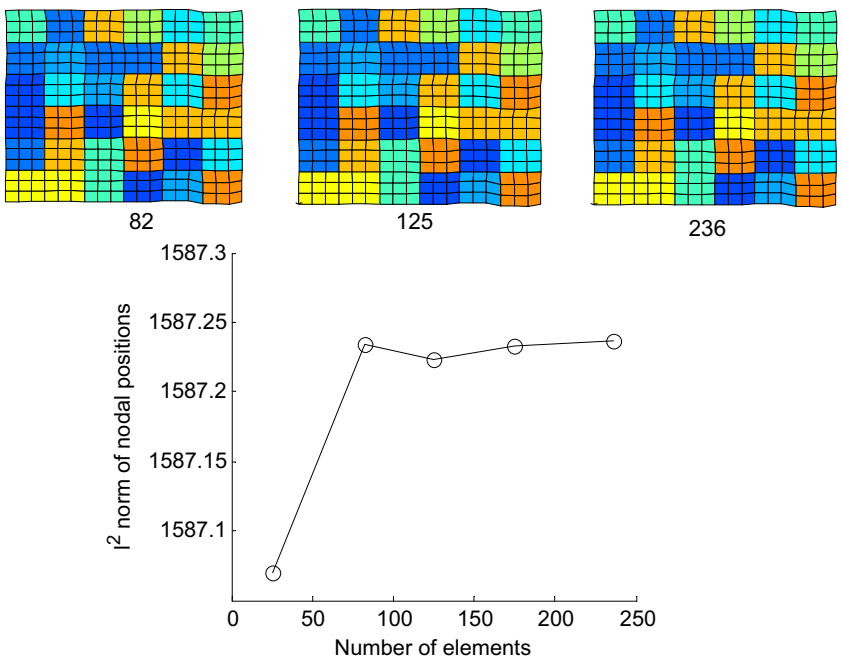

Fig. 10. Convergence with respect to r-mesh: the y-axis shows the l_2 norm of the change in nodal coordinates when using the current mesh (compared to the previous coarser mesh). The final microstructure at t = 1 s is also shown for all cases. An 82 element mesh in the r-space was chosen based on this study.

Table 1
Algorithm for COCF evolution.

(1) Initialize meshes $M(g)$, $M(r|g)$ and $M(g'|rg)$ and load probabilities $\mathcal{A}(g)$, $\mathcal{P}(r|g)$ and $\mathcal{F}(g'|(r,g))$ computed from the sampling algorithm
(2) Apply time increment Δt
(3) At current time step:
  (3.1) Calculate $\overline{N}$ from Eq. (41)
  (3.2) Compute and store the Green's function at integration points of r-mesh by solving Eqs. (A.6) and (A.8)
  (3.3) Compute and store $\bar{\boldsymbol{\sigma}}$ at integration points of r-mesh connected to each orientation $\boldsymbol{g}$ using Eq. (46)
  (3.4) Loop over all nodes in mesh $M(\boldsymbol{g})$ and perform convolution of $\bar{\boldsymbol{\sigma}}$ with the Green's function Eq. (45) to compute the velocity gradient at each nodal orientation
(4) Update probabilities:
  (4.1) Call constitutive model to compute reorientation velocities at nodes in the fundamental region (use velocity gradient found in step (3.4))
  (4.2) Update ODF using Eq. (11)
  (4.3) Compute velocity of nodes in meshes $M(r|g)$ using Eq. (23) and deform the $M(r|g)$ meshes
  (4.4) Compute $\widehat{\mathcal{P}}(\boldsymbol{r}|\boldsymbol{g})$ using Eq. (13) and then, compute $\widehat{\mathcal{P}}(\boldsymbol{r})$ using Eq. (24)
  (4.5) Update COCF $\mathcal{F}(\boldsymbol{g}'|(\boldsymbol{r},\boldsymbol{g}))$ using Eq. (21)
(5) Go to step (2) if time $t < t_{final}$

structure is taken to be of length 100 mm, much larger than the cut-off distance of 25 mm, for computational convenience. A semi-circular mesh is adequate in the r-space owing to the symmetry of the Green's function. For maintaining consistency in the convolution operation in Eq. (42), two r-vectors $+\boldsymbol{r}$ and $-\boldsymbol{r}$ need to be sampled from location $\boldsymbol{g}$ to update the value of COCF weights at nodal location r in the $M_{r|g}$ mesh. Linear interpolation was used in the M_g and $M_{g'|gr}$ meshes with two integration points per element. In the $M_{r|g}$ mesh, four noded quadrilateral elements with bilinear interpolation and four integration points per element were employed.

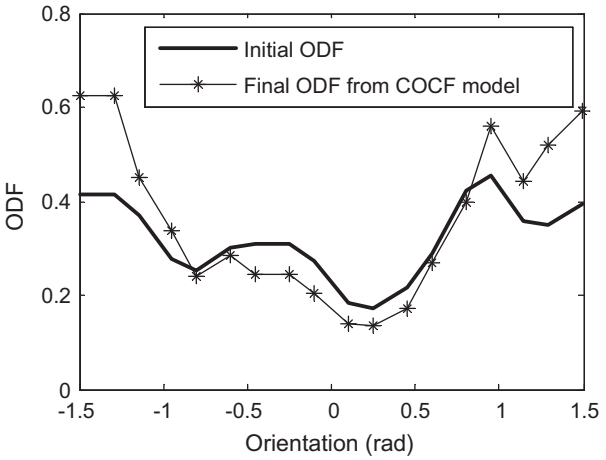

Fig. 11. The final texture predicted by the COCF model is shown. There is strong tendency for crystals with smaller angles (close to the origin) to reorient farther away from the origin. An increase in the ODF close to an ideal orientation of $\theta = \pm\pi/2$ is seen.

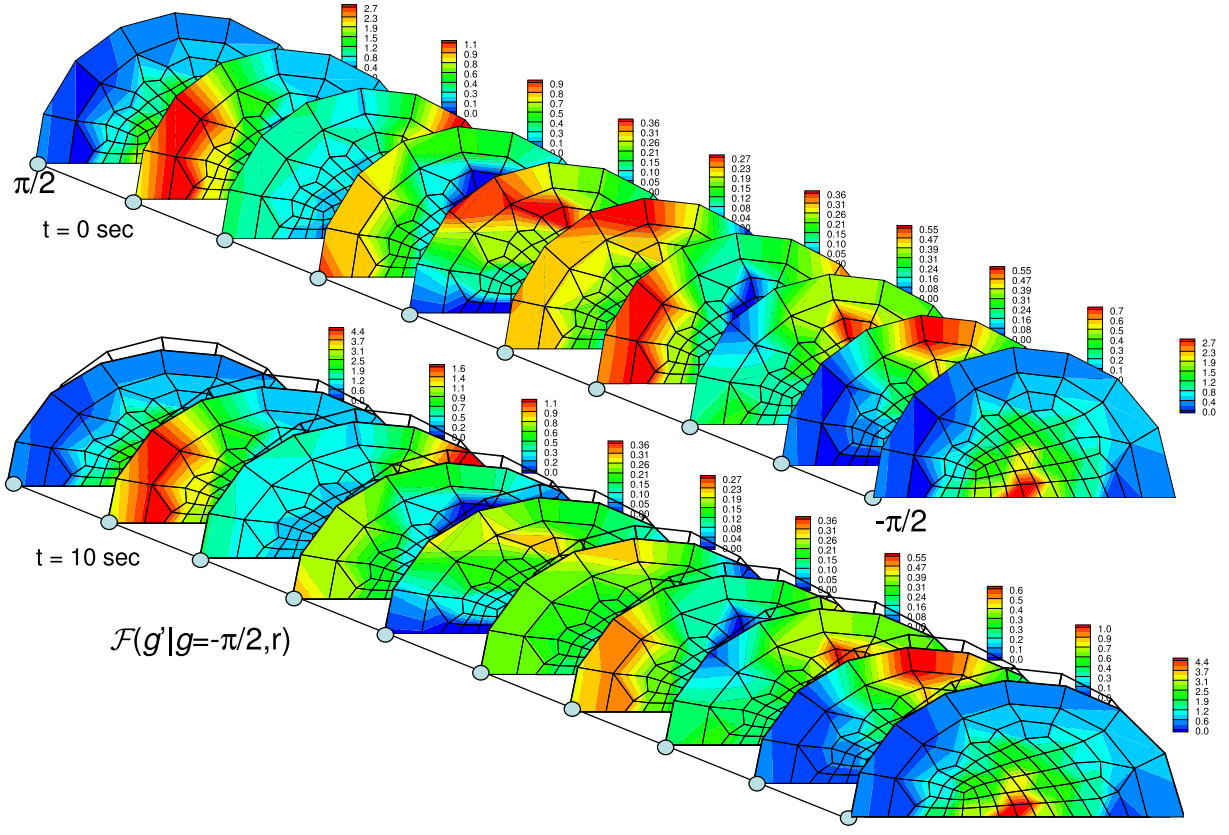

Fig. 12. Visualization of Lagrangian COCF $\widehat{F}(\boldsymbol{g}'|(\boldsymbol{g}=-\pi/2,\boldsymbol{r}))$: the circles correspond to various values of $\boldsymbol{g}'$ from $(-\pi/2, \pi/2)$. The probability density of orientations $\boldsymbol{g}'$ at various distances $\boldsymbol{r}$ from orientation $\boldsymbol{g}=-\pi/2$ is shown over the r-mesh. The first mesh corresponds to $\widehat{F}(\boldsymbol{g}'=-\pi/2|(\boldsymbol{g}=-\pi/2,\boldsymbol{r}))$, the second mesh corresponds to $\widehat{F}(\boldsymbol{g}'=-0.39\pi|(\boldsymbol{g}=-\pi/2,\boldsymbol{r}))$, etc. The evolved COCF at $t=1$ s is also shown.

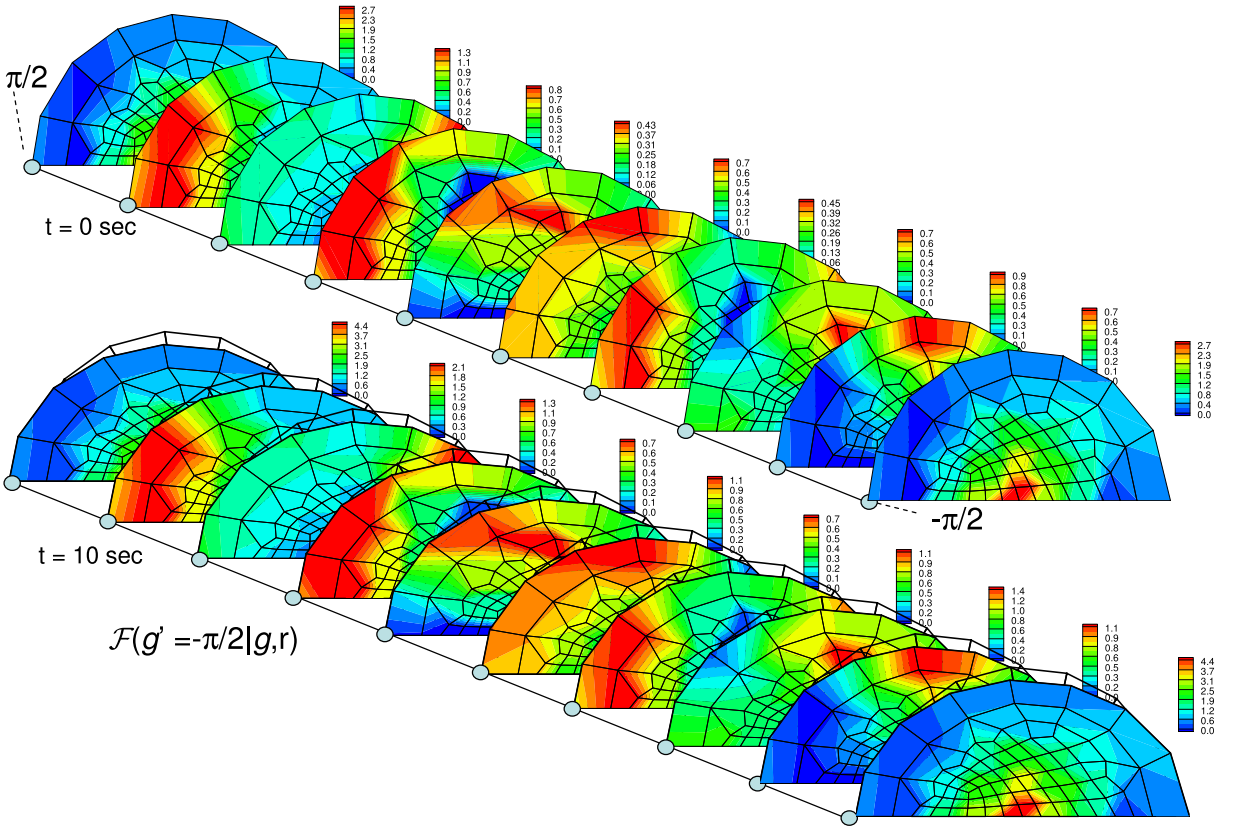

Fig. 13. Visualization of Lagrangian COCF $\widehat{F}(\boldsymbol{g}' = -\pi/2|(\boldsymbol{g},\boldsymbol{r}))$: the circles correspond to various values of $\boldsymbol{g}$ from $(-\pi/2, \pi/2)$. The probability density of orientation $\boldsymbol{g}' = -\pi/2$ at various distances $\boldsymbol{r}$ from orientations $\boldsymbol{g}$ is shown over the r-mesh. The evolved COCF at $t = 1$ s is also shown. The COCF shown here is closely related to that shown in Fig. 12 through the switching symmetry.

Finite element integration techniques (where quantities are summed at gauss points) are used to compute integrals such as Eqs. (22) and (42). This approach circumvents the issue of singularity of Green's functions at $\boldsymbol{r} - \boldsymbol{r}' = 0$ since Gauss points do not fall at this location[2]However, smaller elements are needed close to the singularity to capture the sharp changes in the Green's function close to $\boldsymbol{r} - \boldsymbol{r}' = 0$. For this purpose, a convergence study was performed to select the best possible mesh in the $M_{r|g}$ space that allows good trade-off between computational speed and accuracy. Fig. 9 depicts various different meshes ($M_{r|g}$) used for testing the convergence of the Green's function approach. The Green's function shown in Fig. 6 is superposed on these meshes as a color contour. The meshes were adapted to capture the major variations in Green's function that occur at small values of $\boldsymbol{r} - \boldsymbol{r}'$.

In order to test the approach, an aggregate model was developed where a mesh in the r-space (a full circular mesh) is directly utilized at every integration point in the aggregate RVE to compute the local velocity gradients in the crystals. The approach is similar to the work of Lebensohn (2001) and Lee et al. (2011), except that Green's function convolution is performed in the real space instead of the k-space. A first order correction (Eq. (46)) is used similar to the COCF model. This approach, called the 'aggregate model', is more accurate than the COCF model as it explicitly includes the neighborhood of each crystal rather than an 'average' neighborhood computed during COCF sampling. The convergence results are shown in Fig. 10. The y-axis shows the l_2 norm of the change in nodal coordinates when using the current mesh (compared to the previous coarser mesh). The final microstructure at $t = 1$ s is also shown for a few cases. An 82 element mesh in the r-space was chosen based on this study. We also tested the singularity averaging approach (Kroner, 1987, see footnote 3) and found the change to be modest, with less than 4% change in the Green's function term for orientation $\boldsymbol{g} = -\pi/2$.

The algorithm for the COCF update is given in Table 1. In the algorithm, we first compute the velocity gradient of each orientation $\boldsymbol{g}$ using the Green's function approach. Subsequently, the velocity gradient is used to compute the reorientation

[2] A proper solution to the singularity problem is to construct solutions for a finite small volume V_c surrounding point $\boldsymbol{r}$, then calculate the average value of the velocity gradient to replace the value at $\boldsymbol{r}$ (Kroner, 1987). The average value of velocity gradient $\boldsymbol{L}^0(\boldsymbol{g}^*)$ is given as:

$$\boldsymbol{L}^0(\boldsymbol{g}^*) = \overline{L} + \frac{1}{V_c}\int_{r\in V_c} G(\boldsymbol{r}-\boldsymbol{r}') * \langle \tilde{\sigma}(\boldsymbol{r}')\rangle_{\boldsymbol{g}(r)=\boldsymbol{g}^*} d\boldsymbol{r}. \tag{50}$$

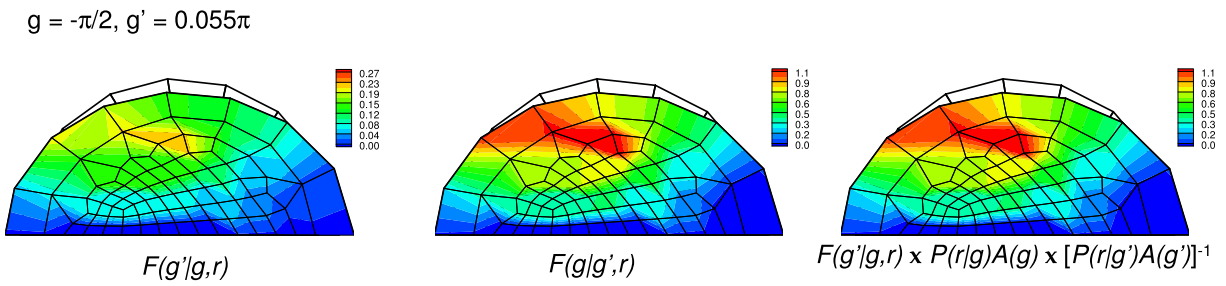

Fig. 14. Switching symmetry of the COCF at $t = 1$ s: the COCF $\widehat{F}(\boldsymbol{g}' = 0.055\pi|(\boldsymbol{g} = -0.5\pi, \boldsymbol{r}))$ can be seen to be equal to $\widehat{F}(\boldsymbol{g}' = -0.5\pi|(\boldsymbol{g} = 0.055\pi, \boldsymbol{r}))$ after multiplying it with the scaling factor $\frac{\mathcal{P}(\boldsymbol{r}|\boldsymbol{g})\mathcal{A}(\boldsymbol{g})}{\mathcal{P}(\boldsymbol{r}|\boldsymbol{g}')\mathcal{A}(\boldsymbol{g}')}$.

velocities in the $M(g)$ mesh and the nodal displacements in $M(r|g)$ meshes. The results are used to compute the Jacobians necessary to update the COCF. A total lagrangian approach is used where the fundamental region mesh for $\boldsymbol{g}$ and $\boldsymbol{g}'$ remain unchanged and the reorientations are only stored at the nodal points. If the reorientations are used to move the nodal locations, new orientation spaces are obtained, which are also valid fundamental regions (Kumar and Dawson, 1996a). Several ideas from the finite element community were used to solve the COCF evolution problem. For example, shape functions were used to calculate the gradient of deformation and the Jacobians, integrations were performed at the integration points to compute integrals (e.g. in Eqs. (22)–(24), (41), (45)), interpolations are performed using shape functions to transfer deformation from nodes to integration points, smoothing is performed to transfer the computed Jacobians from integration points to nodes. The total Lagrangian approach used in this work was found to be adequate up to a strain of 0.2. At larger strains, the

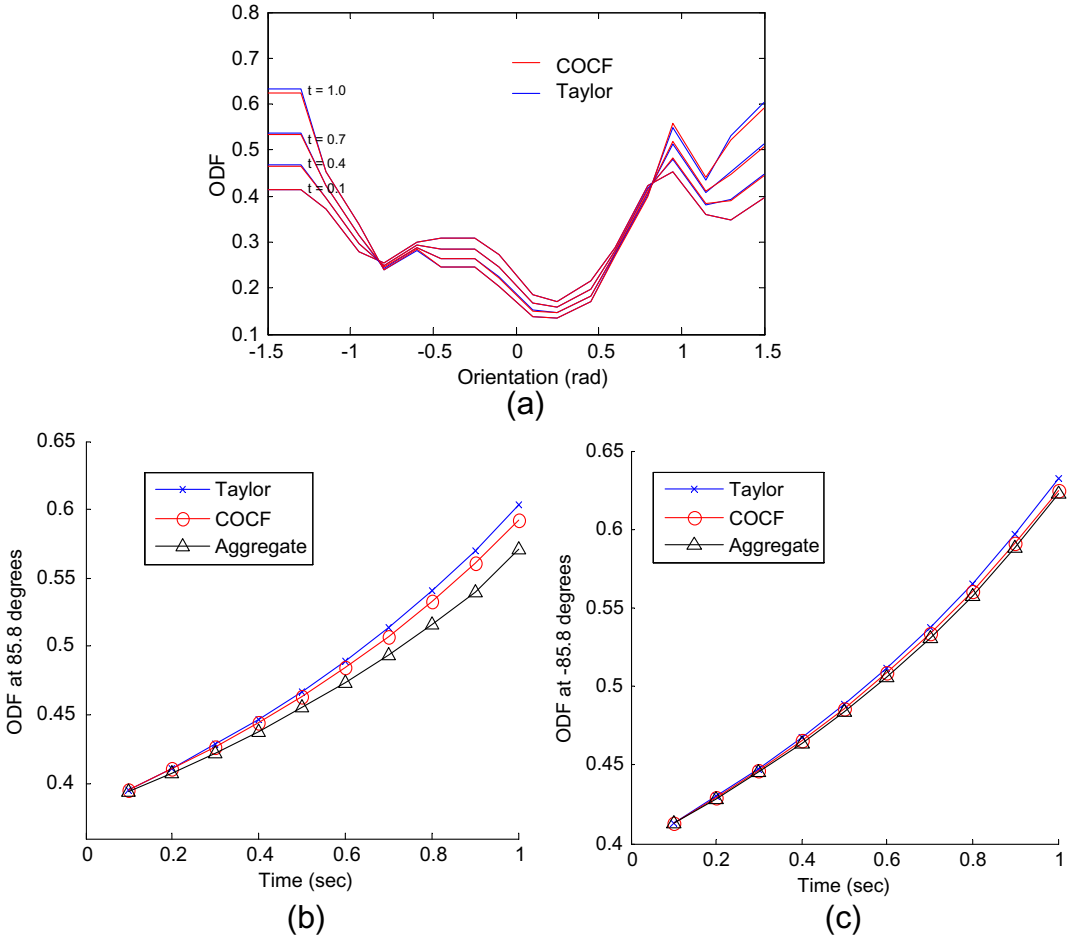

Fig. 15. (a) Comparison of the Lagrangian ODF predicted by the Taylor and COCF model at times $t = 0.1$, 0.4, 0.7 and 1.0 s. (b, c) The ODF values at ±85.8° predicted by the Taylor and COCF models are compared with that predicted by the aggregate model.

nodal points may begin to overlap and interpenetrate. To address such situations, remeshing techniques and updated lagrangian methods need to be developed in the future.

The final texture predicted by the COCF model for the microstructure at $t = 1$ s is shown in Fig. 11. From Kumar and Dawson (1996b), it is seen that texture from tension process leads to an orientation sink at zero degrees and source at $\pm\pi/2$; with the basin of the sink spanning all of orientation space. Thus the ODF will evolve exponentially with strain and eventually approach the asymptote, $A(r) = \delta(r - \pi/2)$. As seen in Fig. 11, there is tendency for crystals with angles close to the origin to reorient farther away (sink) and an associated increase in the ODF close to the ideal orientation of $\theta = \pm\pi/2$ (source) as expected.

The initial Lagrangian COCF $\widehat{F}(\boldsymbol{g}'|(\boldsymbol{g} = -\pi/2, \boldsymbol{r}))$ and the COCF calculated at $t = 1$ s is shown in Fig. 12. In this visualization, probability density of various orientations $\boldsymbol{g}'$ at distances $\boldsymbol{r}$ from orientation $\boldsymbol{g} = -\pi/2$ is shown over the r-mesh. At $t = 0$, the figure shows the average neighborhood of grain with orientation $\boldsymbol{g} = -\pi/2$ as computed from the sampling algorithm. The circles shown in the line connecting various $M(r|g)$ (semi-circle) meshes correspond to various values of $\boldsymbol{g}'$ from $(-\pi/2, \pi/2)$. Thus, the first mesh corresponds to the probability of finding orientation $\boldsymbol{g}' = -\pi/2$ at various distances r from orientation $\boldsymbol{g} = -\pi/2$, given as $\widehat{F}(\boldsymbol{g}' = -\pi/2|(\boldsymbol{g} = -\pi/2, \boldsymbol{r}))$. The second mesh corresponds to $\widehat{F}(\boldsymbol{g}' = -0.39\pi|(\boldsymbol{g} = -\pi/2, \boldsymbol{r}))$, etc. At $r = 0$, a delta function is obtained $\widehat{F}(\boldsymbol{g}'|(\boldsymbol{g} = -\pi/2, \boldsymbol{r} = 0))$ with a large value (seen at node with $\boldsymbol{r} = 0$) in the first mesh and zeros at the same node in the other meshes (not shown). The evolved COCF at a strain of 0.1 is also shown.

The next figure (Fig. 13) shows another facet of the COCF $\widehat{F}(\boldsymbol{g}' = -\pi/2|(\boldsymbol{g}, \boldsymbol{r}))$. Here, the representation depicts the probability of finding orientation $\boldsymbol{g}' = -\pi/2$ in the neighborhood of all other nodal orientations. The circles correspond to various values of $\boldsymbol{g}$ from $(-\pi/2, \pi/2)$. The COCF shown here is closely related to that shown in Fig. 12 through the switching symmetry. Recall the equation for switching symmetry in this context $\mathcal{F}(\boldsymbol{g}' = -\pi/2|(\boldsymbol{g}, \boldsymbol{r})) = \mathcal{F}(\boldsymbol{g}|(\boldsymbol{g}' = -\pi/2, \boldsymbol{r}))\frac{\mathcal{P}(\boldsymbol{r}|\boldsymbol{g}'=-\pi/2)\mathcal{A}(\boldsymbol{g}'=-\pi/2)}{\mathcal{P}(\boldsymbol{r}|\boldsymbol{g})\mathcal{A}(\boldsymbol{g})}$. Note that the ratio of geometrical probabilities $(\mathcal{P})$ is not significantly different from the initial value of one under the mod-

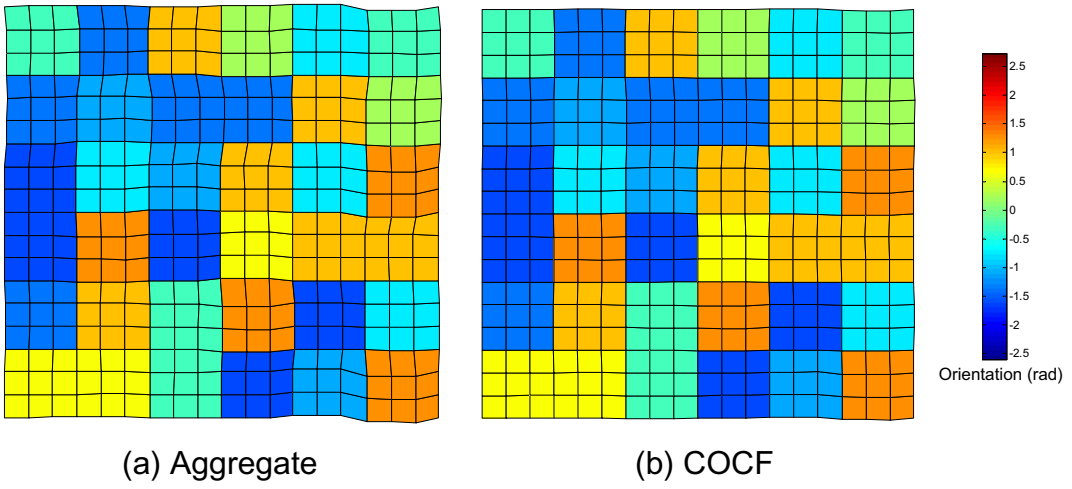

Fig. 16. Direct comparison of the microstructure predicted by (a) aggregate and (b) COCF model. The average velocity gradient predicted by the COCF model (for each orientation) is used to update the microstructure mesh.

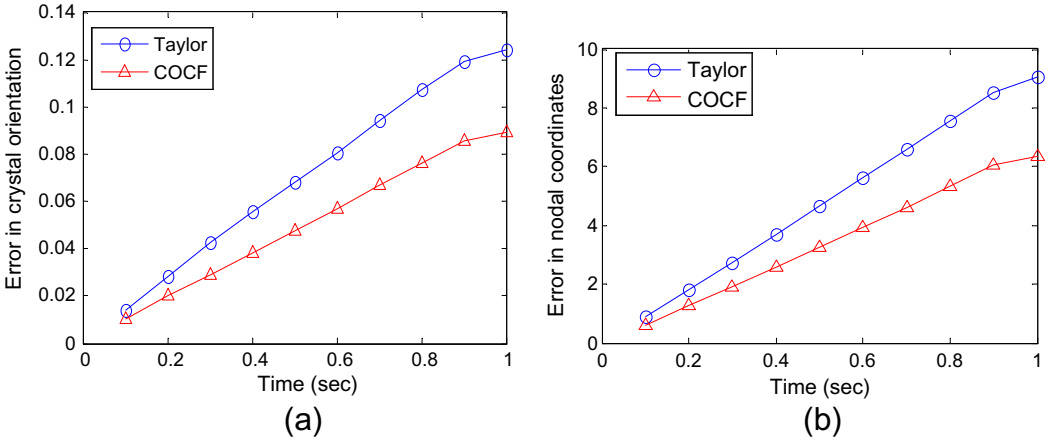

Fig. 17. Comparison of error in (a) crystal orientations and (b) nodal coordinates that arise in Taylor and COCF models. The errors correspond to l^2 norm of the difference in values between Taylor/COCF models with respect to the aggregate model. Errors are plotted as a function of simulation time.

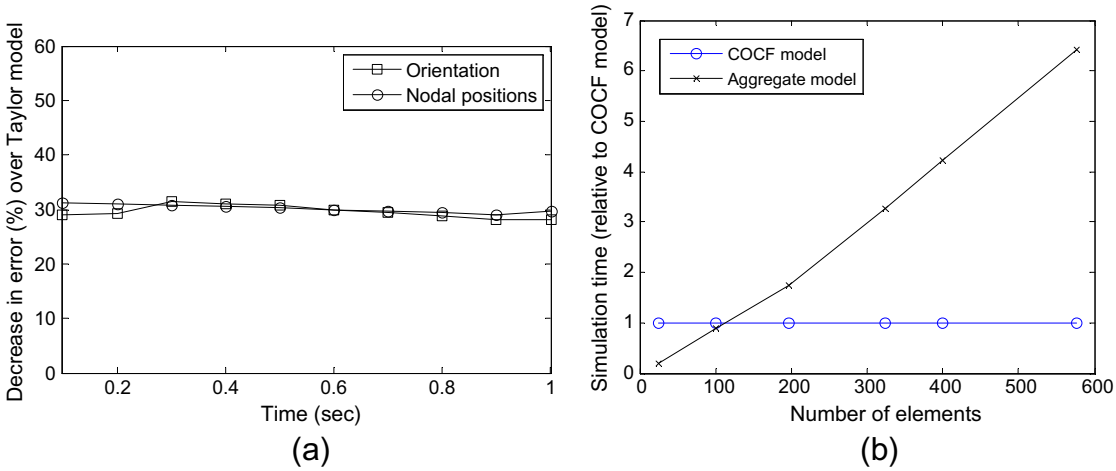

Fig. 18. (a) COCF model reduces the error in prediction of displacements and orientations by 30% when compared to the Taylor model. (b) Comparison of computational speed of aggregate model with respect to COCF model as number of elements in RVE increases.

erate strain imposed here. Since the ODF at $g = -\pi/2$ at $t = 10$ s is larger than ODF at any other orientation (from Fig. 11), this would imply that the COCF $\widehat{F}(\boldsymbol{g}' = -\pi/2|(\boldsymbol{g}, \boldsymbol{r}))$ in Fig. 13 (at $t = 10$ s) will be larger than the COCF shown in Fig. 12. This was used as a quick check to ensure that the switching symmetry is indeed satisfied during the simulation. Fig. 14 demonstrates the switching symmetry in more detail where the COCF $\widehat{F}(\boldsymbol{g}' = 0.055\pi|(\boldsymbol{g} = -0.5\pi, \boldsymbol{r}))$ can be seen to be the same as $\widehat{F}(\boldsymbol{g}' = -0.5\pi|(\boldsymbol{g} = 0.055\pi, \boldsymbol{r}))$ after multiplying it with the scaling factor.

A comparison of the ODF predicted by the Taylor and COCF model at various times are shown in Fig. 15. The Taylor model predicts a sharper ODF at the location of the source ($\boldsymbol{g} = \pi/2$) as expected (Sundararaghavan and Zabaras, 2006). The ODF values for crystals with an orientation close to the location of the source (±85.8°) as predicted by the Taylor and COCF models are directly compared with that sampled from the aggregate model in Fig. 15(b and c). In both cases, the Taylor model predicts the largest ODF. The COCF model predicts an ODF that falls in between those predicted by the Taylor model and the aggregate model.

In order to visually interpret the results of the COCF model, we performed a direct comparison of the microstructure predicted by aggregate and COCF models in Fig. 16. In the case of COCF model, the average velocity gradients predicted for each orientation (from Eq. (45)) were used to update the microstructure mesh. In addition, crystal orientations are also updated. Compared to the aggregate model, COCF approach is seen to give less pronounced deviations of intergranular strains from the applied macroscopic strain. However, the modes of deformation predicted in each crystal is close to those given by the aggregate model. Lower strains are primarily due to the fact that the COCF uses an average neighborhood for each orientation. In other words, it overlooks the differences in local neighborhood if two or more crystals have the same orientation but are at different locations. Alternately, the COCF results shown here can be seen as an ensemble average obtained for all microstructures with the given initial two-point descriptor. In contrast, the aggregate solution shown here provides a single sample from this large ensemble of microstructures. The crystal orientations and displacements predicted by Taylor and COCF models (in Fig. 16) were analyzed with respect to those predicted by the aggregate model. Fig. 17 shows the evolution of error in prediction of orientations and displacements as a function of time. The y-axes correspond to the l^2 norm of the difference in nodal values between Taylor/COCF meshes with respect to the aggregate mesh. The Taylor model gives a larger error in both orientation and displacement compared to the COCF model.

Fig. 18(a) shows that the use of COCF information reduces the error in prediction of displacements and orientations by 30% when compared to the Taylor model. The %age improvement remained almost constant for all strains over the simulation. More importantly, the 30% improvement in error is achieved with a significantly less computational cost compared to the aggregate model. The COCF simulation for the test case was three times faster than the aggregate simulation. As shown in Fig. 18(b), the computational time is significantly lower than a full aggregate model as the number of element increases. The simulation time for the COCF model is independent of the size of the RVE since the statistics are represented over the same COCF mesh for all cases. However, as the number of elements in the RVE increases, the computational expense in aggregate models increase as $O(N^2)$. The improvement in computational efficiency achieved by COCF models is most useful when performing multiscale design of industrial forming processes (e.g. our work in Sundararaghavan and Zabaras (2008)). Once the initial COCF of the raw material (or preform) is known, the data can be used to perform more accurate multiscale simulations without resorting to the use of less accurate Taylor-based or computationally expensive FE-based microstructural models.

6. Conclusion

In this paper, a probabilistic model based on conditional orientation correlation function (COCF) is used for describing microstructure evolution during deformation. The COCF approach is an attempted move towards a new regime of compu-

tation where instead of microstructures, probabilistic descriptors are represented and evolved using finite element analysis. The COCF describes the probability density of occurrence of a crystal orientation $\boldsymbol{g}'$ at a distance $\boldsymbol{r}$ from a given orientation $\boldsymbol{g}$. As the microstructure evolves, the reoriented neighborhood and strain field close to an orientation ($\boldsymbol{g}$) is captured by updating the probability fields in a finite element mesh of the fundamental region of crystal orientation ($\boldsymbol{g}'$) attached to a mesh of distance vectors ($\mathbf{r}$). A novel total Lagrangian approach was developed to perform the probability update that allows evolution of probability densities while satisfying normalization constraints and symmetries.

In contrast to volume fraction (ODF) based models that do not use neighborhood information, COCF-based models capture length scales associated with the actual microstructure and include information about the neighborhood of each crystal orientation. Thus, non-local interactions that lead to complex grain boundary evolution during loading may be statistically captured (using Green's functions). In contrast, Taylor models do not model equilibrium across grain boundaries. Finite element (FE) models with complete microstructural input can capture this effect, however, FE techniques are not of practical use in multiscale simulations due to large computational cost involved in modeling realistic microstructures.

Simulations comparing Taylor, COCF and aggregate models were presented for the case of deformation of a planar (2D) microstructure. Our simulation results indicate that the COCF model decreases the error in prediction of texture and strain by about 30%. The differences between a full microstructure simulation and a COCF-based simulation was primarily attributed to the fact that two-point descriptors contain an average neighborhood for each orientation. In other words, the differences in local neighborhood for two or more crystals with the same orientation that may be present at different locations is overlooked. Thus, the COCF model gives a more constrained solution than the actual deformation, but is less constrained than the deformation predicted by the one-point descriptor (e.g. ODF/Taylor model) that has no neighborhood information. At larger strains, the fundamental region may get severely distorted and remeshing methods still need to be developed. In contrast to finite element methods for which simulation time increases with the size of the RVE, the simulation time is practically constant with the size or discretization of the microstructure. For realistic microstructures, the COCF approach is expected to be significantly faster than FE approaches. In the future, we plan to extend the approach to 3D orientation spaces (FCC, HCP crystals) to address the well-known limitations of Taylor models, and to problems involving twinning (e.g. Abdolvand et al., 2011).

Acknowledgements

The work presented here was funded by a National Science Foundation CAREER Grant (Dr. G. Paulino, Program Manager). Constructive comments were gratefully received from Dr. William Mullins (Office of Naval Research).

Appendix A. Computation of Green's function

The Green's function can be obtained numerically for a general form of $\overline{\boldsymbol{N}}$ from the governing equations (Eq. (40)):

$$\overline{N}_{ijkl}L_{kl,j} - p_{,i} = -[\widetilde{N}_{ijkl}L_{kl}]_{,j} \tag{A.1}$$

$$L_{ii} = 0 \tag{A.2}$$

The Green's functions $G_{ij}(\boldsymbol{r}-\boldsymbol{r}')$ and $H_k(\boldsymbol{r}-\boldsymbol{r}')$ are solutions to the following equations:

$$\overline{N}_{ijkl}G_{km,lj}(\boldsymbol{r}-\boldsymbol{r}') - H_{m,i}(\boldsymbol{r}-\boldsymbol{r}') = -\delta_{im}\delta(\boldsymbol{r}-\boldsymbol{r}') \tag{A.3}$$

$$G_{im,i}(\boldsymbol{r}-\boldsymbol{r}') = 0 \tag{A.4}$$

The Green's functions are obtained from the Fourier transform of the above equations:

$$-\overline{N}_{ijkl}k_jk_l\overline{G}_{km}(\boldsymbol{k}) - ik_i\overline{H}_m(\boldsymbol{k}) = -\delta_{im} \tag{A.5}$$

$$k_k\overline{G}_{km}(\boldsymbol{k}) = 0 \tag{A.6}$$

The above set of linear equations are solved in the k-space and then an inverse Fourier transform is used to compute the Green's functions that are required for computing the velocity gradient and pressure[3]:

$$G_{ij,kl}(\boldsymbol{r}-\boldsymbol{r}') = \frac{-1}{8\pi^3}\int_{\boldsymbol{k}\in K^3} k_kk_l\overline{G}_{ij}(\boldsymbol{k})e^{-i\boldsymbol{k}\cdot(\boldsymbol{r}-\boldsymbol{r}')}dk^3 \tag{A.7}$$

$$H_{m,i}(\boldsymbol{r}-\boldsymbol{r}') = \frac{-i}{8\pi^3}\int_{\boldsymbol{k}\in K^3} k_i\overline{H}_m(\boldsymbol{k})e^{-i\boldsymbol{k}\cdot(\boldsymbol{r}-\boldsymbol{r}')}dk^3 \tag{A.8}$$

[3] The pressure is given by the expression $p(\boldsymbol{r}) = \bar{p} + \int_{r'\in V} H_{i,j}(\boldsymbol{r}-\boldsymbol{r}')\widetilde{N}_{ijkl}L_{kl}d\boldsymbol{r}'^3$. In the statistical COCF model, pressure is obtained using the expression

$$p(\boldsymbol{g}) = \bar{p} + \boldsymbol{H}(\boldsymbol{r}-\boldsymbol{r}') * \left[\int \mathcal{F}(\boldsymbol{g}'|(\boldsymbol{r}-\boldsymbol{r}',\boldsymbol{g}))\widetilde{\boldsymbol{N}}(\boldsymbol{L}(\boldsymbol{g}'),\boldsymbol{g}')\boldsymbol{L}(\boldsymbol{g}')d\boldsymbol{g}'\right]$$

Here components of $\boldsymbol{H}(\boldsymbol{r}-\boldsymbol{r}')$ are $H_{i,j}(\boldsymbol{r}-\boldsymbol{r}')$.

Remark 2. If $\overline{\boldsymbol{N}}$ is taken to be of the following form (this corresponds to an isotropic incompressible matrix):

$$\overline{N}_{ijkl} = \frac{\mu}{2}(\delta_{ik}\delta_{jl} + \delta_{il}\delta_{jk}) \tag{A.9}$$

Then, the Green functions (in k-space) are known analytically:

$$G_{ni}(\boldsymbol{k}) = \frac{2}{\mu k^2}\delta_{ni} - \frac{2}{\mu k^4}k_n k_i \tag{A.10}$$

$$H_m(\boldsymbol{k}) = \frac{i}{k^2}k_m \tag{A.11}$$

where k is the magnitude of wave vector k.

References

Abdolvand, H., Daymond, M.R., Mareau, C., 2011. Incorporation of twinning into a crystal plasticity finite element model: evolution of lattice strains and texture in Zircaloy-2. Int. J. Plasticity. 27 (11), 1721–1738.

Adams, B.L., Canova, G.R., Molinari, A., 1989. A statistical formulation of viscoplastic behavior in heterogeneous polycrystals. Textures Microstruct. 11, 57–71.

Adams, B.L., Boehler, J.P., Guidi, M., Onat, E.T., 1992. Group theory and representation of microstructure and mechanical behavior of polycrystals. J. Mech. Phys. Solids 40, 723–737.

Adams, B.L., Gao, X., Kalidindi, S.R., 2005. Finite approximations to the second-order properties closure in single phase polycrystals. Acta Mater. 53 (13), 3563–3577.

Allison, J., Backman, D., Christodoulou, L., 2006. Integrated computational materials engineering: a new paradigm for the global materials profession journal of the minerals. Metals Mater. Soc. 58 (11), 25–27.

Asaro, R.J., Needleman, A., 1985. Texture development and strain hardening in rate dependent polycrystals. Acta Metall. 33, 923–953.

Beaudoin, A.J., Mecking, H., Kocks, U.F., 1996. Development of localized orientation gradients in fcc polycrystals. Philos. Mag. A 73, 1503–1518.

Becker, R., Panchanadeeswaran, S., 1995. Effects of grain interactions on deformation and local texture in polycrystals. Acta Metall. Mater. 43, 2701–2719.

Beran, M.J., 1968. Statistical Continuum Theories. Interscience Publishers, New York.

Beran, M.J., Mason, T.A., Adams, B.L., Olson, T., 1996. Bounding elastic constants of an orthotropic polycrystal from measurements of the microstructure. J. Mech. Phys. Solids 44, 1543–1563.

Bronkhorst, C.A., Kalidindi, S.R., Anand, L., 1992. Polycrystalline plasticity and the evolution of crystallographic texture in fcc metals. Philos. Trans. R. Soc. Lond. A 341, 443–477.

Bunge, H.J., 1982. Texture Analysis in Materials Science. Butterworth, London.

Clement, A., 1982. Prediction of deformation texture using a physical principle of conservation. Mater. Sci. Eng. 55, 203–210.

Corson, P.B., 1976. Correlation functions for predicting properties of heterogeneous materials. II. Empirical construction of spatial correlation functions for two phase solids. J. Appl. Phys. 45, 3165–3170.

Garmestani, H., Lin, S., Adams, B.L., Ahzi, S., 2001. Statistical continuum theory for large plastic deformation of polycrystalline materials. J. Mech. Phys. Solids 49 (3), 589–607.

Harren, S.V., Asaro, R.J., 1989. Nonuniform deformations in polycrystals and aspects of the validity of the Taylor model. J. Mech. Phys. Solids 37, 191–232.

Kalidindi, S.R., Duvvuru, H.K., 2005. Spectral methods for capturing crystallographic texture evolution during large plastic strains in metals. Acta Mater. 53 (13), 3613–3623.

Kocks, U.F., Tomé, C.N., Wenk, H.R., 2000. Texture and Anisotropy-preferred Orientations in Polycrystals and their Effect on Materials Properties. Cambridge University Press, Cambridge.

Kroner, E., 1987. Modelling Small Deformation of Polycrystals. In: Gittus, J., Zarka, J. (Eds.). Elsevier/Applied Science, New York, p. 229.

Kumar, A., Dawson, P.R., 1996a. The simulation of texture evolution using finite elements over orientation space. I. Development. Comput. Methods Appl. Mech. Eng. 130, 227–246.

Kumar, A., Dawson, P.R., 1996b. The simulation of texture evolution using finite elements over orientation space. II. Application to planar crystals. Comput. Methods Appl. Mech. Eng. 130, 247–261.

Lebensohn, R.A., 2001. N-site modeling of a 3d viscoplastic polycrystal using fast fourier transform. Acta Mater. 49, 2723–2737.

Lee, S.-B., Lebensohn, R.A., Rollett, A.D., 2011. Modeling the viscoplastic micromechanical response of two-phase materials using Fast Fourier Transforms. Int. J. Plasticity 27 (5), 707–727.

McDowell, D.L., 2010. A perspective on trends in multiscale plasticity. Int. J. Plasticity 26 (9), 1280–1309.

Mikdam, A., Makradi, A., Ahzi, S., Garmestani, H., Li, D.S., Remond, Y., 2009. A new approximation for the three-point probability function. Int. J. Solids Struct. 46 (21), 3782–3787.

Molinari, A., Canova, G.R., Ahzi, S., 1987. A self consistent approach of the large deformation polycrystal viscoplasticity. Acta Metall. 35, 2983–2994.

Qidwai, M.A.S., Lewis, A.C., Geltmacher, A.B., 2009. Using image-based computational modeling to study microstructure-yield correlations in metals. Acta Mater. 57 (14), 4233–4247.

Sarma, G.B., Radhakrishnan, B., Dawson, P.R., 2002. Mesoscale modeling of microstructure and texture evolution during deformation processing of metals. Adv. Eng. Mater. 4, 509–514.

Sundararaghavan, V., Zabaras, N., 2006. Design of microstructure-sensitive properties in elasto-viscoplastic polycrystals using multi-scale homogenization. Int. J. Plasticity 22, 1799–1824.

Sundararaghavan, V., Zabaras, N., 2007. Linear analysis of texture-property relationships using process-based representations of Rodrigues space. Acta Mater. 55 (5), 1573–1587.

Sundararaghavan, V., Zabaras, N., 2008. A multi-length scale continuum sensitivity analysis for the control of texture-dependent properties in deformation processing. Int. J. Plasticity 24, 1581–1605.

Taylor, G.I., 1938. Plastic strain in metals. J. Inst. Metals 62, 307–325.

Torquato, S., 2002. Random Heterogeneous Materials: Microstructure and Macroscopic Properties. Springer-Verlag, New York.

Was, G.S., Thaveeprungsriporn, V., Crawford, D.C., 1998. Grain boundary misorientation effects on creep and cracking in Ni-based alloys. J. Metals 50, 44–49.